

# Constraining Quasar and IGM Properties Through Bubble Detection in Redshifted 21-cm Maps

Suman Majumdar<sup>1\*</sup>, Somnath Bharadwaj<sup>1†</sup> and T. Roy Choudhury<sup>2,3‡</sup>

<sup>1</sup>*Department of Physics and Meteorology & Centre for Theoretical Studies, IIT, Kharagpur 721302, India*

<sup>2</sup>*Harish-Chandra Research Institute, Chhatnag Road, Jhusi, Allahabad 211019, India*

<sup>3</sup>*National Centre for Radio Astrophysics, TIFR, Post Bag 3, Ganeshkhind, Pune 411007, India*

7 November 2018

## ABSTRACT

The infrared detection of a  $z > 7$  quasar (Mortlock et al., 2011) has opened up a window to directly probe the inter-galactic medium (IGM) during the epoch of reionization. It is anticipated that future observations will yield more quasars extending to higher redshifts. In this paper we theoretically consider the possibility of detecting the ionized bubble around a  $z = 8$  quasar using targeted redshifted 21-cm observations with the GMRT. The apparent shape and size of the ionized bubble, as seen by a distant observer, depends on the parameters  $\dot{N}_{phs}/C$ ,  $x_{H\text{I}}/C$  and  $\tau_Q$  where  $\dot{N}_{phs}$  and  $\tau_Q$  are respectively the ionizing photon emission rate and age of the quasar, and  $x_{H\text{I}}$  and  $C$  are respectively the neutral fraction and clumping factor of the IGM. The 21-cm detection of an ionized bubble, thus, holds the promise of allowing us to probe the quasar and IGM properties at  $z = 8$ .

In the current work we have analytically calculated the apparent shape and size of a quasar’s ionized bubble assuming an uniform IGM and ignoring other ionizing sources besides the quasar, and used this as a template for matched filter bubble search with the GMRT visibility data. We have assumed that  $\dot{N}_{phs}$  is known from the observed infrared spectrum, and  $C = 30$  from theoretical considerations, which gives us the two free parameters  $x_{H\text{I}}$  and  $\tau_Q$  for bubble detection. Considering 1, 000 hr of observation, we find that there is a reasonably large region of parameter space bounded within  $(x_{H\text{I}}, (\tau_Q/10^7 \text{ yr})) = (1.0, 0.5)$  and  $(0.2, 7.0)$  where a  $3\sigma$  detection is possible if  $(\dot{N}_{phs}/10^{57} \text{ sec}^{-1}) = 3$ . The available region increases if  $\dot{N}_{phs}$  is larger, whereas we need  $x_{H\text{I}} \geq 0.4$  and  $(\tau_Q/10^7 \text{ yr}) \geq 2.0$  if  $(\dot{N}_{phs}/10^{57} \text{ sec}^{-1}) = 1.3$ . Considering parameter estimation, we find that in many cases it will be possible to quite accurately constrain  $\tau_Q$  and place a lower limit on  $x_{H\text{I}}$  with 1, 000 hr of observation, particularly if the bubble is in the early stage of growth and we have a very luminous quasar or a high neutral fraction. Deeper follow up observations (4, 000 and 9, 000 hr) can be used to further tighten the constraints on  $\tau_Q$  and  $x_{H\text{I}}$ . We find that the estimated  $x_{H\text{I}}$  is affected by uncertainty in the assumed value of  $C$ . The quasar’s age  $\tau_Q$  however is robust and is unaffected by the uncertainty in  $C$ .

The presence of other ionizing sources and inhomogeneities in the IGM distort the shape and size of the quasar’s ionized bubble. This is a potential impediment for bubble detection and parameter estimation. We have used the semi-numerical technique to simulate the apparent shape and size of quasar ionized bubbles incorporating these effects. If we consider a 9, 000 hr observation with the GMRT we find that the estimated parameters  $\tau_Q$  and  $x_{H\text{I}}$  are expected to be within the statistical uncertainties.

**Key words:** methods: data analysis - cosmology: theory: - diffuse radiation

## 1 INTRODUCTION

The epoch of reionization is one of the least known periods in the history of our Universe. According to the present understanding, reionization of neutral hydrogen (H I) is an extended process spanning over the redshift range  $6 \lesssim z \lesssim 15$  (Mitra et al., 2011). The intergalactic medium (IGM) during this period is char-

\* E-mail: sumanm@phy.iitkgp.ernet.in

† E-mail: somnath@phy.iitkgp.ernet.in

‡ E-mail: tirth@hri.res.in

acterised by bubbles of ionized hydrogen (H II), centred around luminous sources. Stars forming within early galaxies are believed to be the major sources of ionizing photons during this era (for reviews see Choudhury & Ferrara 2006; Choudhury 2009). Quasars are expected to be very rare during this epoch, but they are capable of generating larger H II bubbles around them with respect to their stellar counterpart. Detection of these H II bubbles will directly probe the state of the local IGM around the ionizing sources. It will also constrain the properties of the quasar, such as its luminosity and age.

The highest redshift at which a quasar has been detected till date is  $z = 7.085$  (Mortlock et al., 2011). The Ly- $\alpha$  absorption spectrum of this object reveals a highly ionized near zone of radius  $2.1 \pm 0.1$  Mpc (physical). The observed near zone size is unexpectedly small when compared with the other high redshift quasars observed in the redshift range  $6.0 < z < 6.4$  (Fan et al., 2003; Willott et al., 2007, 2010). The ionizing photon emission rate estimated for this quasar is  $1.3 \times 10^{57} \text{sec}^{-1}$  assuming a power law for the unabsorbed continuum emission blueward of Ly- $\alpha$  line. The quasar's age ( $\tau_Q$ ) and local volume averaged neutral fraction ( $\langle x_{\text{H I}} \rangle_V$ ) can be estimated from the size of the quasar's near zone, however the estimated  $\tau_Q$  and  $\langle x_{\text{H I}} \rangle_V$  are strongly correlated. For the same observation Bolton et al. (2011) have constrained the  $\tau_Q$  and  $\langle x_{\text{H I}} \rangle_V$  using simulated Ly- $\alpha$  absorption spectra. This study shows that there are several combinations of the  $\tau_Q$  and  $\langle x_{\text{H I}} \rangle_V$  all of which can reproduce the observed data. They find that the spectrum observed by Mortlock et al. (2011) is consistent with  $\tau_Q \sim 10^6$  yr with either  $\langle x_{\text{H I}} \rangle_V \sim 10^{-4} - 10^{-3}$  provided there is a proximate damped Ly- $\alpha$  absorber (DLA) or  $\langle x_{\text{H I}} \rangle_V \sim 0.1$  without a proximate DLA. The same observation is also consistent with  $\tau_Q \sim 10^7$  yr and either  $\langle x_{\text{H I}} \rangle_V \leq 10^{-4}$  with a proximate DLA or a fully neutral IGM  $\langle x_{\text{H I}} \rangle_V \sim 1$  without a proximate DLA. It is quite clear that observations of Ly- $\alpha$  absorption spectra are limited in their ability to determine the age of the quasar and the local neutral fraction. This limitation essentially arises from two reasons. The first being that the IGM becomes nearly opaque at a very low neutral fraction  $\langle x_{\text{H I}} \rangle_V \approx 10^{-4}$ . It is not possible to distinguish between a neutral fraction of  $10^{-4}$  from a completely neutral medium, and the actual ionized bubble around the quasar may extend far beyond the region inferred from the Ly- $\alpha$  absorption spectra. The second limitation arises from the fact that the Ly- $\alpha$  absorption spectrum is a pencil beam observation along a line of sight (LoS) to the quasar. The presence of a proximate DLA can completely change the interpretation of the spectrum.

The redshifted 21-cm emission from neutral hydrogen in the epoch of reionization is believed to be a powerful tool to detect H II bubbles around quasars. The intensity is directly proportional to the H I density, and it is in principle possible to probe the entire ionization profile of the H II bubble. It may be possible to overcome the limitations of Ly- $\alpha$  absorption spectra using redshifted 21-cm observations, and place better constraints on the quasar parameters and the state of the IGM. This is particularly motivated by the fact that the presently functioning GMRT<sup>1</sup> (Swarup et al., 1991) and LOFAR<sup>2</sup>, and the upcoming MWA<sup>3</sup> and 21CMA<sup>4</sup> are all sensitive to the H I signal from the epoch or reionization. However, redshifted H I observations have their own limitations in that

the H I signal is extremely small relative to the sensitivities of the present and upcoming telescopes. Further, the signal will be buried deep in foregrounds which are a few orders of magnitude larger than the signal (Ali, Bharadwaj & Chengalur, 2008; Bernardi et al., 2009).

Datta, Bharadwaj & Choudhury (2007) (hitherto Paper I) have proposed a matched filter technique to detect ionized bubbles in radio-interferometric observations of redshifted 21-cm emission. The matched filter optimally combines the entire signal of an ionized bubble while minimizing the noise and the foreground contributions. The redshift  $z \sim 8$  is most optimal for bubble detection (Datta, Bharadwaj & Choudhury, 2009), and at this redshift a  $3\sigma$  detection is possible for bubbles of comoving radius larger than 24 and 28 Mpc with 1000 hr of observation using the GMRT and MWA respectively, assuming that the neutral hydrogen fraction is  $\sim 0.6$  outside the bubble. This technique, however, is limited by the density fluctuations in H I outside the bubble, and analytical estimates (Paper I) and simulations (Datta et al., 2008) show that it is not possible to detect bubbles of comoving radius  $\leq 6$  and  $\leq 12$  Mpc using the GMRT and MWA respectively, however large be the observation time.

The matched filter technique mentioned above assumes the H II bubble to be spherical. However, a growing spherical bubble will appear anisotropic along the LoS to a present day observer due to the finite light travel time (FLTT) (Wyithe & Loeb, 2004; Yu, 2005; Wyithe, Loeb & Barnes, 2005; Sethi & Haiman, 2008) and also due to the evolution of global ionization fraction (Geil et al., 2008). In an earlier work (Majumdar et al. (2011); hitherto Paper II), we have analytically quantified this anisotropy and studied the possibility of detecting such a bubble in a targeted search around a known quasar. We find that the bubble appears elongated along the LoS during the early stages of its growth, whereas it appears compressed in the later stages when the growth slows down. In addition to this, the apparent centre of the bubble also shifts towards the observer. We find that a spherical filter is adequate for bubble detection even when the apparent anisotropy of the bubble's shape is taken into account, the centre of the best matched filter will however be shifted relative to the quasar. We also propose that the measured shift and the radius of the best matched filter can together be used to constrain the age and luminosity of the quasar.

In this work we consider the detection of an H II bubble in a targeted 21-cm search centred on a known quasar at  $z = 8$  and we investigate the possibility of using such an observation to constrain the properties of the quasar and the IGM. For this purpose we improve upon the spherical filter by calculating the apparent, anisotropic shape of the quasar bubble and using this as a template for the filter. We expect this to give a better match to the bubble that is actually present in the data. Further, we also expect improved parameter estimation using the improved filter.

Our earlier work (Paper II) was entirely based on analytic estimates which do not take into account the presence of ionizing sources other than the quasar and the inhomogeneities in the IGM. We have overcome this limitation here by using the semi-numerical technique (Choudhury, Haehnelt & Regan, 2009) to simulate the ionization field.

This paper is arranged as follows – In Section 2 we briefly discuss the model for bubble growth around a quasar, and the matched filter technique for detecting such a bubble. We also present the improved filter based on the calculated apparent shape of the bubble. In Section 3 we use analytic estimates, based on the bubble growth equation, to study the SNR for bubble detection. We use this to determine the parameter range where a  $3\sigma$  detection is possible in

<sup>1</sup> <http://www.gmrt.ncra.tifr.res.in>

<sup>2</sup> <http://www.lofar.org/>

<sup>3</sup> <http://www.haystack.mit.edu/ast/arrays/mwa/>

<sup>4</sup> <http://21cma.bao.ac.cn/>

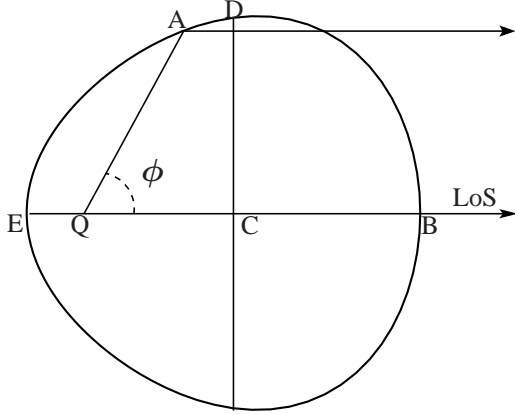


**Figure 1.** This shows the apparent shape of the H II bubble around a quasar Q as seen by a distant observer located in the direction indicated by the arrows. The apparent anisotropy of the H II bubble arises from the fact that photons received from different parts of the bubble had been emitted at different stages of its growth. The apparent centre of the bubble is shifted by  $QC$  from the quasar Q to the point C. The bubble's apparent radius is  $EC = CB = R_{||}$  along the LoS and  $CD = R_{\perp}$  perpendicular to LoS.

1,000 hr of observation with the GMRT. We then consider parameter estimation, and explore the kind of limits that can be placed on the quasar and IGM properties using the matched filter technique. Section 4 briefly describes how we have simulated the apparent shape of quasar bubbles, and we present our results and summarize our findings in Section 5.

Our entire analysis is restricted to the redshift  $z = 8$ . We have used the values from the WMAP 7 year data (Komatsu et al., 2011; Jarosik et al., 2011)  $h = 0.705$ ,  $\Omega_m = 0.2726$ ,  $\Omega_{\Lambda} = 0.726$ ,  $\Omega_b h^2 = 0.0223$  for the cosmological parameters.

## 2 BUBBLE DETECTION

### 2.1 Model for Bubble Growth

The growth of a spherical H II region around a quasar which is isotropically emitting ionizing photons at a rate  $\dot{N}_{phs}$  is governed by the equation (Shapiro & Giroux, 1987; White, Becker, Fan & Strauss, 2003; Wyithe & Loeb, 2004; Wyithe, Loeb & Barnes, 2005; Yu, 2005; Sethi & Haiman, 2008),

$$\frac{4\pi}{3} \frac{d}{dt} (x_{HI} \langle n_H \rangle r^3) = \dot{N}_{phs} - \frac{4}{3} \pi \alpha_B C \langle n_H \rangle^2 r^3, \quad (1)$$

[eq. (1) of Paper II and eq (7) of Yu 2005]. It is assumed that the quasar is triggered at a cosmic time  $t_i$ , and  $\tau = t - t_i$  denotes the quasar's age at any later time  $t$ . The variable  $r(\tau)$  denotes the radius of the spherical ionizing front at the instant when a photon that was emitted from the quasar at  $\tau$  catches up with the ionizing front. The term  $\alpha_B (= 2.6 \times 10^{-13} \text{ cm}^3 \text{ s}^{-1})$  is the recombination coefficient to excited levels of hydrogen at  $T = 10^4 \text{ K}$ ,  $\langle n_H \rangle$  and  $\langle n_{H I} \rangle$  are the average hydrogen and neutral hydrogen densities respectively,  $x_{H I}$  is the neutral fraction of the IGM and  $C \equiv \langle n_{H I}^2 \rangle / \langle n_H \rangle^2$  is the clumping factor which quantifies the effective clumpiness of the hydrogen inside the bubble. Eq. (1) tells us that the growth of the H II bubble is determined by the ionizing photon emission rate after accounting for the photons required to compensate for the recombinations inside the existing ionized region.

For a constant  $\dot{N}_{phs}$  the solution to the above growth model

(eq. (1)) takes the form

$$r(\tau) = r_S \left[ 1 - \exp\left(-\frac{\tau}{\tau_{rec}}\right) \right]^{\frac{1}{3}}, \quad (2)$$

[eq. (2) of Paper II and eq. (8) of Yu 2005] where  $\tau_{rec} = x_{H I} (C \langle n_H \rangle \alpha_B)^{-1}$  and  $r_S = \left( 3 \dot{N}_{phs} \tau_{rec} / (4\pi x_{H I} \langle n_H \rangle) \right)^{1/3}$ . The apparent shape of the growing bubble that is perceived by a present day observer will be distorted due to the fact that photons received by the observer from different parts of the bubble had been emitted at different stages of the bubble's growth (see Figure 1). To visualize this apparent shape one needs the relation between  $r$  and the angle  $\phi$  between the LoS and the point A (Figure 1) under consideration on the ionization front. Consider a quasar observed at an age  $\tau_Q$ . The light travel time starting from the quasar at  $\tau$  to the point A and then to the observer is  $[r(\tau)/c](1 - \cos \phi)$  more compared to the photon that was emitted from the quasar at  $\tau_Q$  and travels straight to the observer. This gives

$$\tau_Q = \tau + \frac{r(\tau)}{c} (1 - \cos \phi), \quad (3)$$

[eq. (7) of Paper II and eq. (3) of Yu 2005]. We use eq. (2) and eq. (3) to determine  $r$  as a function of  $\phi$ . This gives the quasar's apparent shape shown in Figure 1.

The apparent shape of a quasar's H II bubble has been studied in detail in Paper II. We find that the FLTT has two effects, 1. the bubble appears to be anisotropic along the LoS and 2. the bubble's apparent centre shifts along the LoS away from the quasar towards the observer. We now briefly discuss how we parametrize these two effects. Referring to Fig 1, we use  $R_{\perp} = CD$  to quantify the overall comoving size of the bubble. The bubble centre C is located mid way between EB. We use the dimensionless shift parameter  $s$  defined as,

$$s = \frac{QC}{R_{\perp}}, \quad (4)$$

to quantify the shift in the bubble's centre as a fraction of its radius. We find (see Paper II for details) that  $s$  can be greater than 1 during the early stages of the bubble's growth and it approaches 0 in the later stages of evolution.

We use the dimensionless anisotropy parameter  $\eta$  defined as,

$$\eta = \frac{CB}{R_{\perp}} - 1, \quad (5)$$

to quantify the anisotropy in the apparent shape of the bubble. A value  $\eta > 0$  indicates that the bubble is elongated along the LoS and a value  $\eta < 0$ , indicates that it is compressed along the LoS. Our earlier work (Paper II) shows that  $\eta$  has values in the range 0.1 to 0.5 during the early stages of growth when the bubble appears elongated along the LoS. We also find that  $\eta$  has values in the range 0.0 to  $-0.2$  in the later stages of evolution when the bubble may appear compressed along the LoS.

### 2.2 Matched filter bubble detection

The basic observable quantity in the radio interferometry is the visibility  $\mathcal{V}(\vec{U}, \nu)$  which is related to the specific intensity pattern on the sky  $I_{\nu}(\vec{\theta})$  as

$$\mathcal{V}(\vec{U}, \nu) = \int d^2\theta A(\vec{\theta}) I_{\nu}(\vec{\theta}) e^{2\pi i \vec{\theta} \cdot \vec{U}} \quad (6)$$

The baseline  $\vec{U} = \vec{d}/\lambda$  denotes the antenna separation  $\vec{d}$  projected in the plane perpendicular to the LoS in units of the observing

wavelength  $\lambda$ ,  $\vec{\theta}$  is a two dimensional vector in the sky plane with the origin at the centre of the FoV (the phase centre) and  $A(\vec{\theta})$  is the beam pattern of a single antenna. For the GMRT  $A(\vec{\theta})$  can be well approximated by a Gaussian  $A(\vec{\theta}) = e^{-\theta^2/\theta_0^2}$  where  $\theta_0 \approx 0.6 \theta_{\text{FWHM}}$  and we use  $2.28^\circ$  for  $\theta_0$  at 157.77 MHz *i.e.*  $z = 8$ . We consider a situation where the observation is spanned across several frequency channels around the central frequency of 157.77 MHz.

The visibility recorded in a radio-interferometric observation is actually a combination of several contributions,

$$\mathcal{V}(\vec{U}, \nu) = S(\vec{U}, \nu) + HF(\vec{U}, \nu) + N(\vec{U}, \nu) + F(\vec{U}, \nu), \quad (7)$$

where the first term  $S(\vec{U}, \nu)$  is the signal from the ionized region that is actually present in the observational data,  $HF(\vec{U}, \nu)$  is the contribution from fluctuations in the H I distribution outside the ionized bubble,  $N(\vec{U}, \nu)$  is the system noise which is inherent to the measurement and  $F(\vec{U}, \nu)$  is the contribution from astrophysical foregrounds.

The signal  $S(\vec{U}, \nu)$  from an ionized region will appear as a decrement with respect to the background 21-cm radiation. A spherical H II bubble embedded in an uniform IGM with a neutral fraction  $x_{\text{HI}}$  is parametrized by its comoving radius  $R_b$ , the redshift  $z_c$  and the angular position  $\vec{\theta}_c$  corresponding to the centre of the bubble. The quantity  $r_\nu$  is the comoving distance to the redshift where the H I emission received at  $\nu = 1420 \text{ MHz}/(1+z)$  originated, and  $r'_\nu = dr_\nu/d\nu$ . A plane perpendicular to LoS and passing through the centre of the bubble at a comoving distance  $r_\nu$  will cut a disk of comoving radius  $R_\nu = R_b \sqrt{1 - (\Delta\nu/\Delta\nu_b)^2}$  from the bubble, where  $\Delta\nu = \nu_c - \nu$  and  $\Delta\nu_b = R_b/r'_\nu$ , and  $\theta_\nu = R_\nu/r_\nu$  is the angular extent corresponding to  $R_\nu$ . For a bubble located at the centre of the FoV we have,

$$S(\vec{U}, \nu) = -\pi \bar{I}_\nu x_{\text{HI}} \theta_\nu^2 \left[ \frac{2J_1(2\pi U \theta_\nu)}{2\pi U \theta_\nu} \right] \Theta \left( 1 - \frac{|\nu - \nu_c|}{\Delta\nu_b} \right), \quad (8)$$

where  $\bar{I}_\nu = 2.5 \times 10^2 \frac{Jy}{sr} \left( \frac{\Omega_b h^2}{0.02} \right) \left( \frac{0.7}{h} \right) \left( \frac{H_0}{H(z)} \right)$ ,  $\Theta(x)$  is the Heaviside step function, and  $J_1(x)$  is the Bessel function of first order. The expected signal has a peak value (Paper I) of  $S(0, \nu) = 1.12 \text{ mJy}$  for a bubble with  $R_b = 40 \text{ Mpc}$ , and  $S(0, \nu) \propto R_b^2$ .

The expected H I signal is very weak, so much so that the contribution  $HF(\vec{U}, \nu)$  from H I fluctuations outside the bubble may, in some cases, exceed the expected signal. We consider the system noise  $N(\vec{U}, \nu)$  in each baseline and frequency channel to be an independent Gaussian random variable with zero mean and r.m.s.

$$\sqrt{\langle \hat{N}^2 \rangle} = C^x \left( \frac{\Delta\nu}{1 \text{ MHz}} \right)^{-1/2} \left( \frac{\Delta t}{1 \text{ sec}} \right)^{-1/2} \quad (9)$$

where the constant  $C^x$  is different for different interferometric arrays,  $\Delta\nu$  is the channel width and  $\Delta t$  is the correlator integration time. Following Paper I, we use  $C^x = 1.03 \text{ Jy}$  for the GMRT. We note that the r.m.s. noise  $\sqrt{\langle \hat{N}^2 \rangle}$  will actually vary with  $\vec{U}$ , we have ignored this baseline dependence in order to keep the analysis simple. Further we do not expect this to be a very significant effect compared to the various other uncertainties arising from the lack of knowledge about the IGM and the quasar properties. The astrophysical foregrounds  $F(\vec{U}, \nu)$  are expected to be several orders of magnitude larger than the H I signal. But they are predicted to have a featureless, continuum spectra whereas the signal is expected to have a dip around  $\nu_c$  (central frequency of the target H II bubble).

This difference holds the promise of allowing us to separate the signal from the foregrounds.

The visibility based matched filter technique, proposed in Paper I, optimally combines the signal from an ionized region while minimizing the other contributions. In this technique we use the signal expected from a spherical H II bubble centered at redshift  $z_b$  and comoving radius  $R_b$  as a template, and search for the presence of this signal in the data using the estimator,

$$\hat{E}(z_b, R_b) = \sum_{a,b} S_f^*(\vec{U}_a, \nu_b) \hat{\mathcal{V}}(\vec{U}_a, \nu_b). \quad (10)$$

Here  $S_f(\vec{U}, \nu)$  is the filter and  $\hat{\mathcal{V}}(\vec{U}, \nu)$  are the measured visibilities. The filter is defined as,

$$S_f(\vec{U}, \nu) = \left( \frac{\nu}{\nu_c} \right)^2 \left[ S(\vec{U}, \nu) - \frac{\Theta(1 - 2|\nu - \nu_c|/B')}{B'} \int_{\nu_c - B'/2}^{\nu_c + B'/2} S(\vec{U}, \nu') d\nu' \right], \quad (11)$$

where  $S(\vec{U}, \nu)$  is the signal expected from the bubble that we are trying to detect. The filter eliminates any frequency independent component of the foreground from the frequency range  $\nu_c + B'/2$  to  $\nu_c - B'/2$ . All the contributions to  $\mathcal{V}$ , except the signal  $S(\vec{U}, \nu)$ , are assumed to be random variables of zero mean, uncorrelated to the filter whereby the estimator has expectation value,

$$\langle \hat{E} \rangle = \sum_{a,b} S_f^*(\vec{U}_a, \nu_b) S(\vec{U}_a, \nu_b). \quad (12)$$

The other terms in eq. (7) contribute only to the variance,

$$\langle (\Delta \hat{E})^2 \rangle = \langle (\Delta \hat{E})^2 \rangle_{\text{HF}} + \langle (\Delta \hat{E})^2 \rangle_{\text{N}} + \langle (\Delta \hat{E})^2 \rangle_{\text{F}}. \quad (13)$$

The signal to noise ratio for the estimator is

$$\text{SNR} = \frac{\langle \hat{E} \rangle}{\sqrt{\langle (\Delta \hat{E})^2 \rangle}} \quad (14)$$

Matched filter bubble detection is carried out by analyzing the SNR for different values of the filter parameters  $z_f$  and  $R_f$ . We expect the SNR to peak when the filter parameters  $z_f$  and  $R_f$  exactly match the parameters  $z_b$  and  $R_b$  of the bubble that is actually present in the data. We have a statistically significant ( $3\sigma$ ) bubble detection if the peak  $\text{SNR} \geq 3$ . Note that the two angular coordinates  $\theta_x$  and  $\theta_y$  are already known in a targeted search around a quasar. In general,  $\theta_x$  and  $\theta_y$  have also to be treated as free parameters in a blind search.

The filter  $S_f(\vec{U}, \nu)$  is defined in such a way [eq. (11)] that it is insensitive to the presence of a smooth frequency independent foreground component. Under the assumed foreground model (Paper I), the residual foreground contribution  $\langle (\Delta \hat{E})^2 \rangle_{\text{F}}$  is predicted to be much smaller than the other contributions to  $\langle (\Delta \hat{E})^2 \rangle$  and we do not consider it here. In the absence of patchy reionization outside the bubble, the H I fluctuations trace the dark matter fluctuations. This imposes a lower bound  $R_b > 12 \text{ Mpc}$  for the GMRT on the smallest H II bubble that can be detected (Datta et al., 2008). Considering patchy reionization outside the bubble, we expect galaxies to produce ionized regions with a typical radius of 6 Mpc or smaller. The quasar bubbles that we can detect using the GMRT ( $\geq 20 \text{ Mpc}$ ) are much larger than these ionized patches. Earlier work (Datta et al., 2008) shows that the H I fluctuations do not play a very important role if the quasar bubble is much larger than the typical size of the ionized patches outside the bubble, and

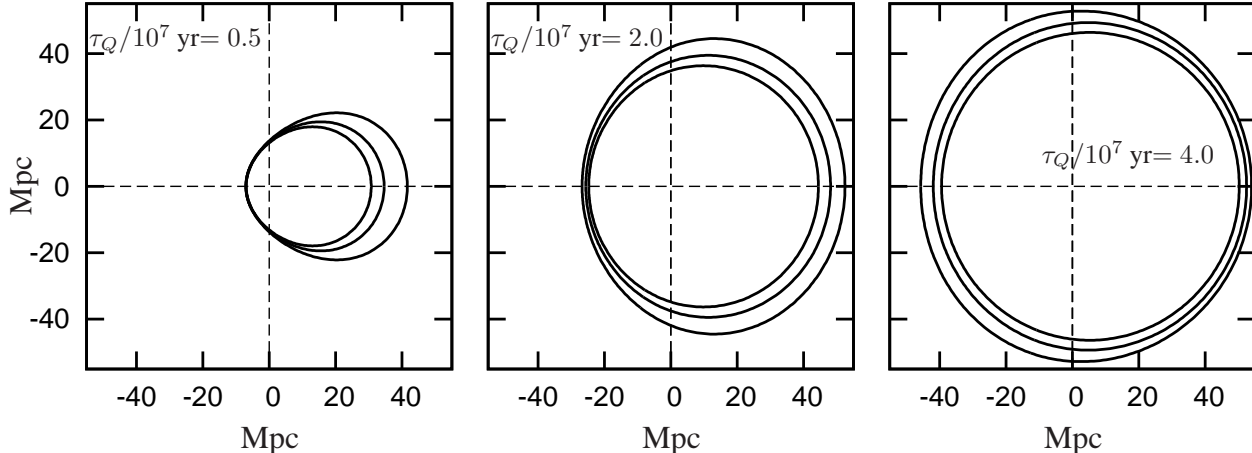


**Figure 2.** This shows the H II bubble around a quasar with  $(\dot{N}_{phs}/10^{57} \text{ sec}^{-1}) = 3$  at different stages of growth  $((\tau_Q/10^7 \text{ yr}) = 0.5, 2.0, 4.0)$ . The three different shapes in each panel correspond to different IGM neutral fractions ( $x_{H\text{I}} = 0.75, 0.50, 0.25$ ), the bubble size increasing with decreasing neutral fraction. Note that  $((\tau_Q/10^7 \text{ yr}) = 2.0)$  corresponds to  $\tau_Q/\tau_{rec} = 1.21$  for  $x_{H\text{I}} = 0.5$  and  $\tau_{rec} \propto x_{H\text{I}}$ . The quasar is at the centre of each panel. The x-axis represents the LoS and the observer is on the right side of the panels.

$\tau_Q/10^7$ (yr)	$x_{H\text{I}}$	$R_{\perp}$ (Mpc)	$\eta$	$s$
0.5	0.75	17.9	0.05	0.66
0.5	0.50	19.4	0.07	0.71
0.5	0.25	22.0	0.11	0.79
2.0	0.75	36.3	-0.05	0.27
2.0	0.50	39.4	-0.07	0.29
2.0	0.25	44.5	-0.11	0.29
4.0	0.75	46.3	-0.03	0.12
4.0	0.50	49.3	-0.04	0.11
4.0	0.25	52.8	-0.06	0.07

**Table 1.** This tabulates the size ( $R_{\perp}$ ), and the anisotropy and shift parameters ( $\eta$  and  $s$  respectively) corresponding to the shapes shown in Figure 2.

we have ignored this contribution in our estimates in this paper. We have only considered the system noise  $\langle(\Delta\hat{E})^2\rangle_N$  which is the most dominant component in  $\langle(\Delta\hat{E})^2\rangle$ . The resulting SNR is inversely proportional to the square root of the total observation time  $\text{SNR} \propto t_{obs}^{1/2}$ .

### 2.3 Anisotropic filter

The matched filter technique considered in earlier works [Paper I; Datta et al. (2008); Datta, Bharadwaj & Choudhury (2009)] and briefly described above uses the signal expected from a spherical H II bubble [eq. (8)] as a template for the filter [eq. (11)]. The actual bubble is however anisotropic due to the FLTT, and we expect a mismatch between the template and the actual signal. We can avoid this if we use the apparent anisotropic shape as the template for the filter  $S_f(\vec{U}, \nu)$ . This is done by numerically determining the bubble radius  $r$  as a function of  $\phi$  (Figure 1) by solving eq. (2) and (3). A section through the anisotropic bubble continues to be a circular disk, and eq. (8) still holds for the signal. The only difference is that the comoving radius  $R_b$  now varies along the LoS, and we

have to use the calculated  $r(\phi)$  instead of a fixed  $R_b$ . An inspection of eq.s (1), (2) and (3) shows that the apparent shape is completely specified by three free parameters  $\dot{N}_{phs}/C$ ,  $x_{H\text{I}}/C$  and  $\tau_Q$ . It is therefore necessary to analyze the SNR for different values of these three parameters and determine the values of  $\dot{N}_{phs}/C$ ,  $x_{H\text{I}}/C$  and  $\tau_Q$  for which the SNR peaks.

Here we consider a targeted search around a known quasar whose infrared spectrum has been measured. It is possible to extrapolate the observed quasar’s infrared spectrum blueward of the Ly- $\alpha$  line and estimate  $\dot{N}_{phs}$  (example Mortlock et al. 2011). It is reasonable to assume that  $\dot{N}_{phs}$  is known in a targeted search for bubble detection. Further, the analysis of numerical simulations indicate that the clumping factor has a value  $C = 30$  at  $z = 8$  (Gnedin & Ostriker, 1997; Yu, 2005; Yu & Lu, 2005). With this assumption the apparent shape of the H II bubble is completely specified by only two parameters the mean neutral fraction  $x_{H\text{I}}$  and  $\tau_Q$  the age of the quasar. Our entire analysis of bubble detection is in terms of these two parameters,  $x_{H\text{I}}$  and  $\tau_Q$ . For a quasar with a constant luminosity  $(\dot{N}_{phs}/10^{57} \text{ sec}^{-1}) = 3$ , Figure 2 shows how the shape and size of the H II bubble vary with  $x_{H\text{I}}$  and  $\tau_Q$ . The bubble grows as  $r(\tau) \propto (\tau/x_{H\text{I}})^{1/3}$  in the early stages when  $\tau \ll \tau_{rec}$  (eq. 2) and saturates at  $r(\tau) = r_s$ , which is independent of  $x_{H\text{I}}$ , when  $\tau/\tau_{rec} \sim 1$ . Figure 2 and Table 1 show that the size of the bubble decreases with increasing  $x_{H\text{I}}$  during the early stage of growth, and this effect becomes less noticeable at the later stage of growth. The bubble appears elongated along the LoS in the early stage, whereas it becomes compressed in the later stage. We see that the size  $R_{\perp}$ , anisotropy  $\eta$  and shift  $s$  all vary with  $\tau_Q$  and  $x_{H\text{I}}$ .

## 3 ANALYTIC ESTIMATES

In this section we present analytic estimates of bubble detection in a targeted search around a known high redshift quasar. For this purpose the H I outside the bubble is assumed to follow the dark matter. For the growth of the quasar bubble we ignore the effect of other ionizing sources and inhomogeneities in the H I distributions. The

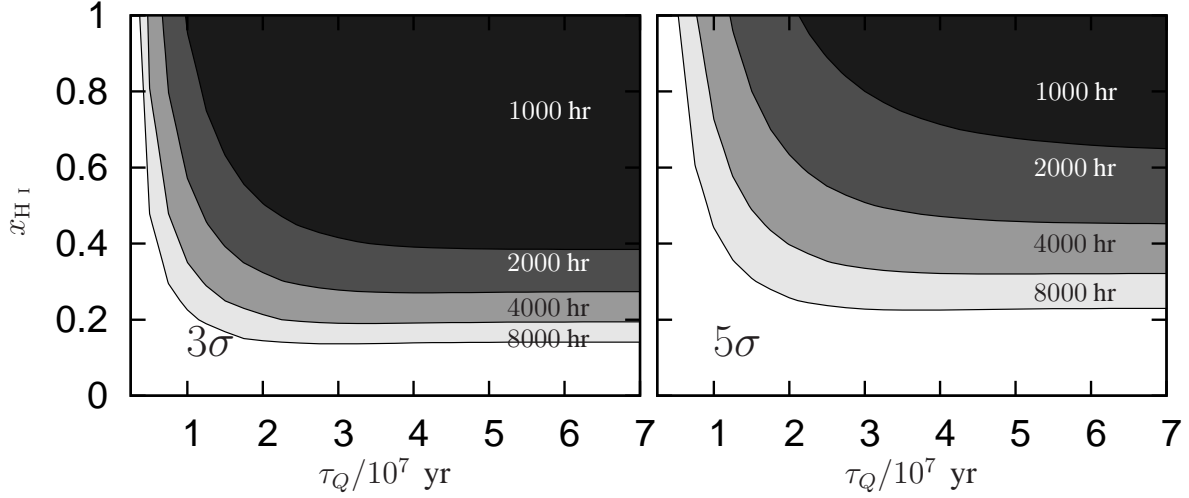


**Figure 3.** This shows the analytic estimates of minimum observation time required for  $3\sigma$  and  $5\sigma$  (left and right panels respectively) detection of the H II bubble around the quasar ULASJ1120+0641 discovered by Mortlock et al. (2011).

bubble’s evolution is assumed to be exactly described by eq. (2) discussed earlier. For bubble detection we use the apparent shape obtained using eqs. (2) and (3) to calculate the filter  $S_f(\vec{U}, \nu)$ . The search has two parameters  $x_{\text{H I}}$  and  $\tau_Q$ , and we expect a perfect match when these have the same value as the bubble actually present in the data.

Quasars typically have a luminosity of around  $\dot{N}_{\text{phs}} \sim 10^{57} \text{ sec}^{-1}$ . The highest redshift quasar detected till date has a luminosity of  $\dot{N}_{\text{phs}} \sim 1.3 \times 10^{57} \text{ sec}^{-1}$  (Mortlock et al., 2011). Very little is known about the luminosity distribution of very high redshift quasars. The more luminous quasars are expected to produce larger ionized bubbles, and the prospect of a 21-cm detection is also expected to be higher for a more luminous quasar. In much of our analysis we have used two different quasar luminosities  $\dot{N}_{\text{phs}} = 3 \times 10^{57} \text{ sec}^{-1}$  and  $8 \times 10^{57} \text{ sec}^{-1}$ . The typical quasar age is expected to be in the range  $10^6 - 10^8$  yrs (Haehnelt et al., 1998; Haiman & Hui, 2001). The analysis of the proximity zones in the Ly- $\alpha$  spectra of high redshift quasars yield quasar ages which are larger than  $1 - 3 \times 10^7$  yrs (Worseck & Wisotzki, 2006; Lu & Yu, 2011). We have considered quasar ages in the range  $10^6 - 10^8$  yrs in our analysis.

### 3.1 Detectability

We first consider the possibility of detecting the H II bubble around the quasar ULASJ1120+0641 (Mortlock et al., 2011) using GMRT redshifted 21-cm observation. The size and shape of the H II bubble depend on  $x_{\text{H I}}$  and  $\tau_Q$ , and we have determined the observation time that will be required for different values of these parameters. The left and right panels of Figure 3 show the observation time that will be required for a  $3\sigma$  and  $5\sigma$  detection respectively. We find that for 1,000 hr of observation a  $3\sigma$  detection is possible in a considerable region of parameter space where  $x_{\text{H I}} > 0.4$  and  $(\tau_Q/10^7 \text{ yr}) > 1.5$ , and a  $5\sigma$  detection is possible in a relatively smaller region of parameter space where  $x_{\text{H I}} > 0.7$  and  $(\tau_Q/10^7 \text{ yr}) > 3.5$ . A  $3\sigma$  detection is possible for a considerably large region of the parameter space ( $x_{\text{H I}} > 0.2$  and  $(\tau_Q/10^7 \text{ yr}) > 1.0$ ) with 4,000 hr of observation, and we require

approximately 8,000 hr of observation for a  $5\sigma$  detection in this region of parameter space.

The possibility of a 21-cm detection is quite favourable if the quasar luminosity is of the order of  $\dot{N}_{\text{phs}} = 3 \times 10^{57} \text{ sec}^{-1}$  or larger, and in much our analysis we use two different quasar luminosities  $\dot{N}_{\text{phs}} = 3 \times 10^{57} \text{ sec}^{-1}$  and  $8 \times 10^{57} \text{ sec}^{-1}$ . Here we present estimates of the SNR for bubble detection considering 1000 hr of GMRT observation around a known quasar. The right panels in Figure 4 show the peak SNR, which corresponds to the situation when the filter and the signal are exactly matched. And the left panels in Figure 4 show the corresponding quasar bubble size ( $R_{\perp}$  in Mpc). An ionized bubble grows as  $r(\tau) \propto (\tau \dot{N}_{\text{phs}}/x_{\text{H I}})^{1/3}$  in the early stages when  $\tau \ll \tau_{\text{rec}}$  (eq. 2) and saturates at,

$$r(\tau) = r_s = 54 \text{ Mpc} \left( \frac{\dot{N}_{\text{phs}}}{3 \times 10^{57} \text{ sec}^{-1}} \right)^{1/3}, \quad (15)$$

for

$$\tau > \tau_{\text{rec}} = 3.3 \times 10^7 \text{ yr } x_{\text{H I}}^{-1}. \quad (16)$$

We see that both these stages are distinctly visible in the apparent size of the H II bubble shown in Figure 4. Note that the value of  $r_s$  where the growth saturates, is independent of  $x_{\text{H I}}$ .

The SNR from an H II bubble scales as  $x_{\text{H I}} R_b^{3/2} \dot{N}_{\text{phs}}^{1/3}$  (Paper I), which implies that  $\text{SNR} \propto (x_{\text{H I}} \tau \dot{N}_{\text{phs}})^{1/2}$  when  $\tau \ll \tau_{\text{rec}}$  and  $\text{SNR} \propto x_{\text{H I}} \dot{N}_{\text{phs}}^{1/2}$  and independent of  $\tau$  when  $\tau > \tau_{\text{rec}}$ .

We observe that the SNR contours are roughly hyperbolas in the  $x_{\text{H I}} - \tau_Q$  plane, and the hyperbolas flatten out at large  $\tau$ . We mainly focus on the SNR=3 contour, a  $3\sigma$  (or higher) detection is possible in the parameter region to the right of this contour. We first consider the case where  $(\dot{N}_{\text{phs}}/10^{57} \text{ sec}^{-1}) = 3$ . We find that a  $3\sigma$  detection is possible over a reasonably large region of the parameter space. For a high neutral fraction ( $0.6 \leq x_{\text{H I}}$ ), it will be possible to detect an H II bubble even if it is small ( $R_{\perp} \approx 20$  Mpc) and in an early stage of its growth ( $\tau_Q/10^7 \text{ yr} \geq 0.5$ ). However, it will not be possible to detect the bubble if the quasar’s age ( $\tau_Q/10^7 \text{ yr}$ ) is less than 0.5, even if the IGM is completely neutral outside the bubble. In contrast, a  $3\sigma$  detection is possible for a low neutral fraction only if the bubble is very large and in a later stage of its evolution. The

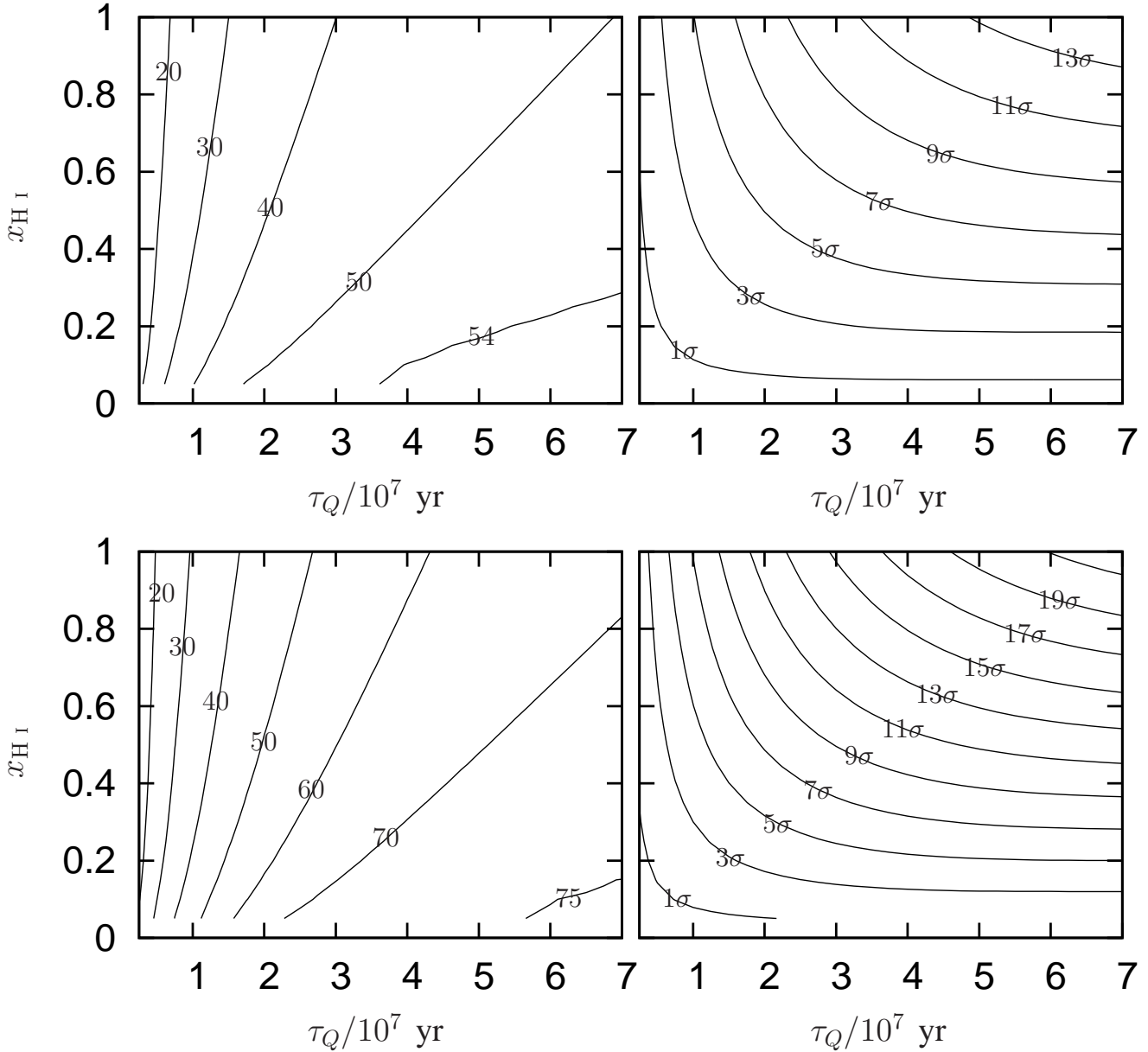


**Figure 4.** This shows analytic estimates of the bubble’s comoving size ( $R_{\perp}$  in Mpc)(Left panel) and the SNR for the best matched filter (Right panel). Top and bottom panels correspond to quasar photon emission rates of ( $\dot{N}_{phs}/10^{57} \text{ sec}^{-1}$ ) = 3 and 8 respectively.

lowest neutral fraction where a  $3\sigma$  detection is possible is  $x_{\text{HI}} \approx 0.2$ . The quasar’s age should be  $\sim 3.0 \times 10^7$  yr (or more) for which the bubble radius is  $R_{\perp} \sim 45$  Mpc. For a quasar of this luminosity, a  $3\sigma$  detection is not possible if the neutral fraction is lower than 0.2. We find that a  $5\sigma$  detection also is possible for a reasonably large region of the parameter space roughly covering  $x_{\text{HI}} > 0.3$  and  $(\tau_Q/10^7 \text{ yr}) > 1$ .

We next consider the case where  $(\dot{N}_{phs}/10^{57} \text{ sec}^{-1}) = 8$ . The scaling behaviour discussed earlier leads us to expect that  $R_{\perp}$  and the SNR will increase by a factor of 1.38 and 1.63 respectively if  $(\dot{N}_{phs}/10^{57} \text{ sec}^{-1})$  is increased from 3 to 8. Note however that, the scaling relations actually hold for the bubble seen from the rest frame of the quasar, and we do not expect them to be exactly valid for the bubble’s apparent shape when the FLTT is taken into account. The effect of FLTT is expected to be larger for

$(\dot{N}_{phs}/10^{57} \text{ sec}^{-1}) = 8$  where the bubble is predicted to be larger in comparison to  $(\dot{N}_{phs}/10^{57} \text{ sec}^{-1}) = 3$ .

We see that there is an increase in the region of parameter space where a  $3\sigma$  detection is possible for the more luminous quasar. The smallest age for which a  $3\sigma$  detection is possible is now reduced to  $(\tau_Q/10^7 \text{ yr}) = 0.3$  compared to 0.5 when  $(\dot{N}_{phs}/10^{57} \text{ sec}^{-1}) = 3$ . This however requires a completely neutral IGM. It is not possible to detect the bubble if the quasar’s age  $(\tau_Q/10^7 \text{ yr})$  is less than 0.3, even if the IGM is completely neutral outside the bubble. At the other end, a  $3\sigma$  detection is possible if the neutral fraction is  $\approx 0.1$ , provided the quasar’s age is  $2.5 \times 10^7$  yr or more. For a quasar of this luminosity, it is not possible to detect bubbles if the neutral fraction is less than 0.1.

There are indications that the neutral fraction could have a value  $x_{\text{HI}} \approx 0.5$  at  $z = 8$  (Mitra et al., 2011). For this neutral

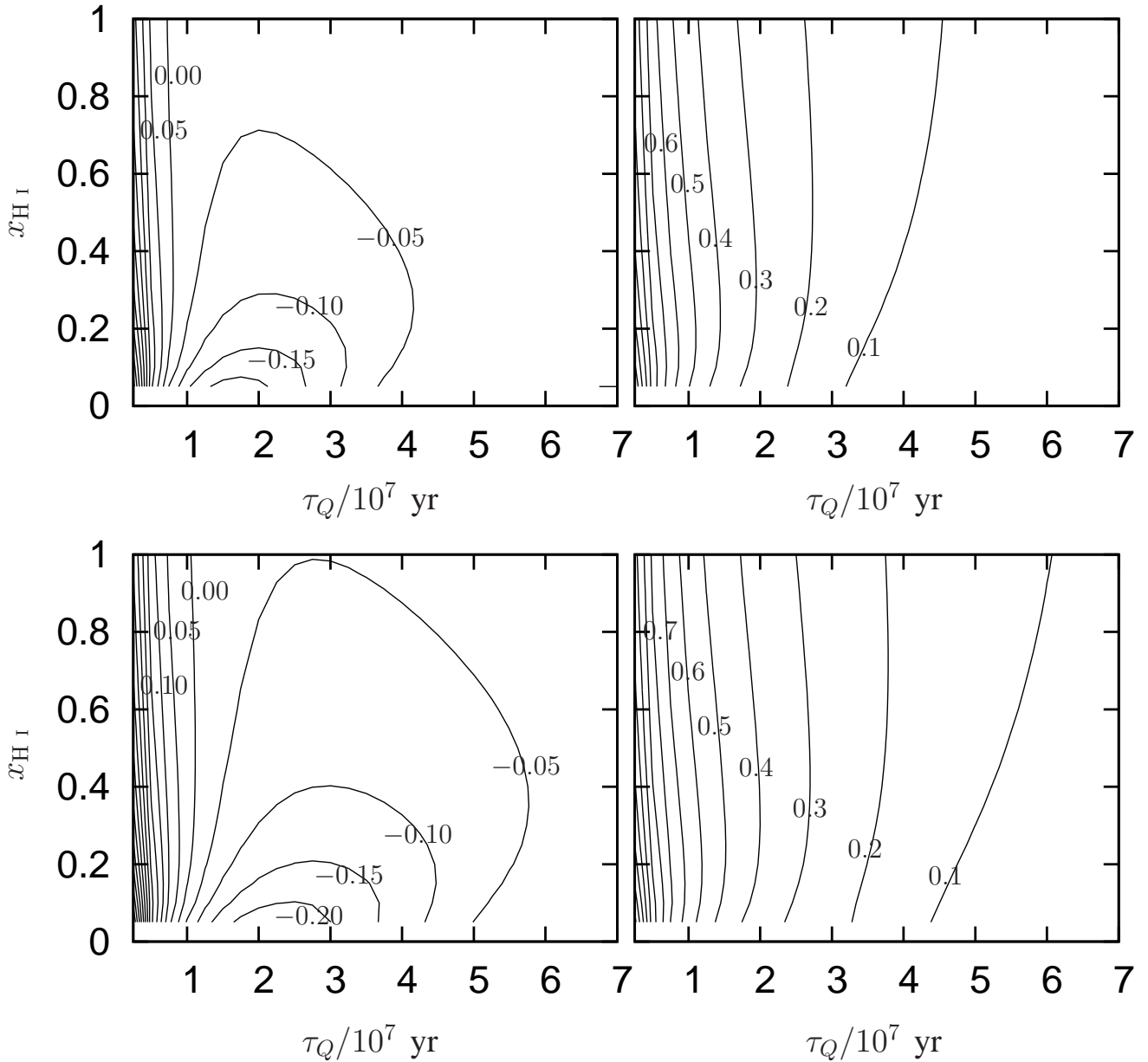


**Figure 5.** This shows analytic estimates of the anisotropy parameter  $\eta$  (Left panel) and the shift parameter  $s$  (Right panel) for the quasar's H II bubble. Top and bottom panels correspond to quasar photon emission rates of ( $\dot{N}_{phs}/10^{57} \text{ sec}^{-1}$ ) = 3 and 8 respectively.

fraction a  $3\sigma$  detection is possible for  $(\tau_Q/10^7 \text{ yr}) \geq 0.75$  and  $0.5$  for  $(\dot{N}_{phs}/10^{57} \text{ sec}^{-1}) = 3$  and  $8$  respectively. The corresponding H II bubble radii are 25 and 30 Mpc in these two cases respectively. We find that a  $5\sigma$  detection is possible provided that the quasar's age exceeds  $(\tau_Q/10^7 \text{ yr}) \geq 2.0$  and  $1.0$  respectively in these two cases.

We note that, the peak SNR does not increase very significantly when we use the anisotropic filter instead of the spherical filter used in earlier works. The anisotropic filter however has the advantage that it parametrises the bubble in terms of  $x_{\text{H I}}$  and  $\tau_Q$  both of which are physically relevant and interesting quantities in their own right. We next consider the possibility of using matched filter technique to observationally determine  $x_{\text{H I}}$  and  $\tau_Q$ .

set	$x_{\text{H I}}$	$\tau_Q/10^7$ (yr)
a0	0.75	1.0
b0	0.75	1.8
c0	0.75	2.8
d0	0.50	1.2
e0	0.50	2.8
f0	0.25	2.8

**Table 2.** This tabulates the quasar and IGM parameters for which we have analytically considered parameter estimation.

### 3.2 Parameter Estimation

Once an H II bubble has been detected in 1,000 hr of GMRT observation around a known quasar, it is natural to explore the possibility

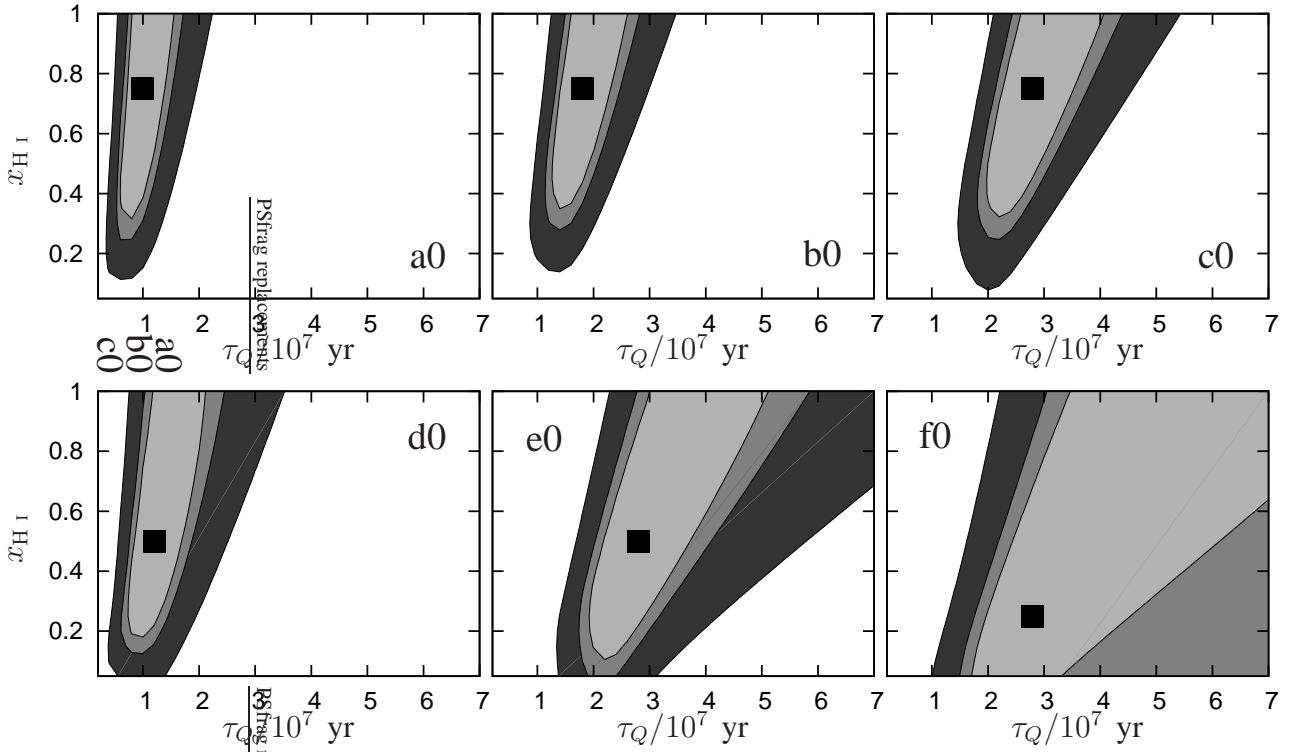


**Figure 6.** This shows the uncertainty ( $\Delta \text{SNR} = 1$ ) in the estimated parameters ( $x_{\text{HI}}$  and  $\tau_Q$ ) for the parameter sets tabulated in Table 2. The three shaded regions correspond to 1, 000, 4, 000 and 9, 000 hr of observations respectively. The quasar photon emission rate is ( $\dot{N}_{\text{phs}}/10^{57} \text{ sec}^{-1}$ ) = 3 in all the panels.

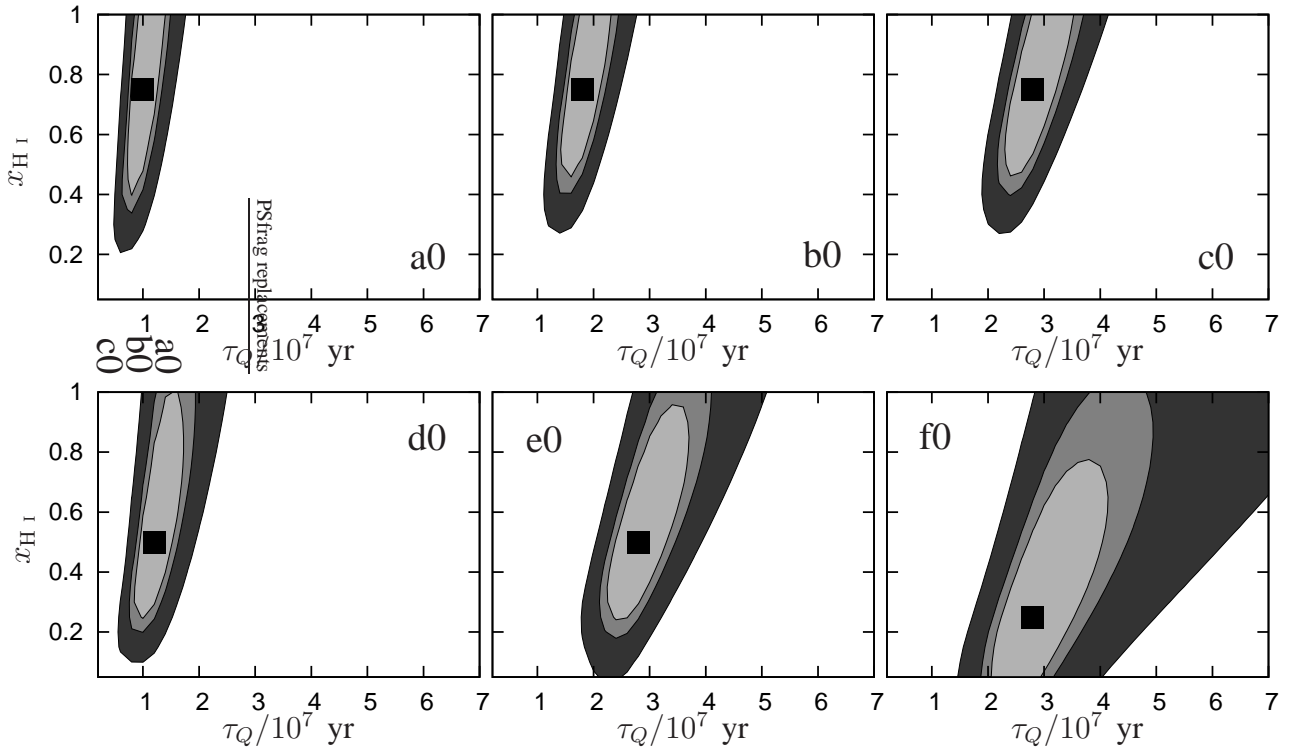


**Figure 7.** Similar to Figure 6 with ( $\dot{N}_{\text{phs}}/10^{57} \text{ sec}^{-1}$ ) = 8.

of using this to estimate the quasar's age and the IGM neutral fraction,  $\tau_Q$  and  $x_{\text{H I}}$  respectively. In most cases the 1,000 hr observation considered earlier is barely adequate for a detection, and we do not expect very significant parameter estimation from such an observation. Here we also consider deeper follow up observations of 4,000 and 9,000 hr specifically carried out for the purpose of parameter estimation once the H II bubble has been detected.

Parameter estimation is based on the idea that  $\tau_Q$  and  $x_{\text{H I}}$  are uniquely imprinted in the H II bubble's apparent size and shape (Figure 2). Here we use  $R_{\perp}$  (Figure 4) to quantify the bubble's apparent size, and  $\eta$  and  $s$ , introduced earlier, to quantify the bubble's apparent shape. Figure 5 shows the behaviour of  $\eta$  and  $s$  for different values of the parameters  $\tau_Q$  and  $x_{\text{H I}}$ . Due to the FLTT the light reaching a present day observer was emitted earlier from the back side of the bubble in comparison to the light coming from the front side. For a bubble in the rapid stage of growth ( $\tau \ll \tau_{\text{rec}}$ ) the back side appears to have a much smaller radius compared to its front side, causing the bubble to appear elongated along the LoS. The centre of the apparent shape of the bubble also shifts towards the observer. Both these features are clearly seen in the parameter range  $(\tau_Q/10^7 \text{ yr}) \leq 1$  (Figure 5) where the bubble appears elongated ( $\eta > 0$ ). We see that both  $\eta$  and  $s$  are extremely sensitive to  $\tau_Q$  in this stage, however we do not see any significant  $x_{\text{H I}}$  dependence. Though much of this region is outside the parameter range where a  $3\sigma$  detection is possible for 1000 hr of GMRT observation. For  $(\dot{N}_{\text{phs}}/10^{57} \text{ sec}^{-1}) = 3$  and 8, there are small regions with high neutral fraction ( $x_{\text{H I}} \geq 0.65$ ) and  $(\tau_Q/10^7 \text{ yr}) > 0.5$  and 0.3 respectively where it may be possible to detect an elongated bubble.

Most of the region  $(\tau_Q/10^7 \text{ yr}) > 1$  of the  $x_{\text{H I}} - \tau_Q$  parameter space where the H II bubble is detectable, corresponds to the late stages of its growth where the bubble appears compressed. The bubble is no longer in the phase of rapid growth, and it appears mildly compressed ( $\eta \leq 0$ ) along the LoS. There is however still a considerable shift in the apparent centre of the bubble in this stage of growth. In this stage the anisotropy  $\eta$  is sensitive to both  $x_{\text{H I}}$  and  $\tau_Q$ . The shift  $s$  is mainly sensitive to  $\tau_Q$  and largely insensitive to  $x_{\text{H I}}$  (Figure 5). The bubble's radius (Figure 4) also is sensitive to both  $x_{\text{H I}}$  and  $\tau_Q$  in this stage of the bubble's growth. The period  $0.6 - 4.0 \times 10^7 \text{ yr}$  which is just after the rapid growth of the bubble appears to be the most suitable for parameter estimation as the apparent size and shape of the bubble are sensitive to both  $\tau_Q$  and  $x_{\text{H I}}$ . The bubble's apparent shape and size are only weakly sensitive to  $\tau_Q$  beyond  $(\tau_Q/10^7 \text{ yr}) > 4.0$ . However, the bubble's size remains sensitive to  $x_{\text{H I}}$ , and it may be possible to constrain this parameter in the very late stage of growth.

Ideally we expect the SNR to peak when the parameters ( $x_{\text{H I}}$ ,  $\tau_Q$ ) of the filter exactly match those of the bubble that is actually present in the data. However the statistical fluctuations will cause the position of the peak to shift introducing an uncertainty in the parameter estimation. We use the criteria  $\Delta\text{SNR} = 1$  to estimate the uncertainty in the estimated values of the parameters  $x_{\text{H I}}$  and  $\tau_Q$ . Table 2 shows the sets of parameters for which we have considered parameter estimation in this section. The parameter sets a0, b0 and c0 have a high neutral fraction ( $x_{\text{H I}} = 0.75$ ), d0 and e0 have  $x_{\text{H I}} = 0.5$  and f0 has a low neutral fraction ( $x_{\text{H I}} = 0.25$ ). Figure 6 and 7 show the uncertainties in parameter estimation for all these cases assuming that  $(\dot{N}_{\text{phs}}/10^{57} \text{ sec}^{-1}) = 3$  and 8 respectively.

There are indications that the neutral fraction could have a value  $x_{\text{H I}} \approx 0.5$  at  $z = 8$  (Mitra et al., 2011). We have considered two sets of parameter values (d0 and e0) for this neutral fraction. Considering 1,000 hr of observation for the set d0, where

the bubble is in its early stage of growth  $(\tau_Q/10^7 \text{ yr}) = 1.2$ , we find that it is possible to put both lower and upper limits on the quasar age  $(0.5 \leq \tau_Q/10^7 \text{ yr}) \leq 3.5$  for a quasar with  $(\dot{N}_{\text{phs}}/10^{57} \text{ sec}^{-1}) = 3$ . In this case no limits on  $x_{\text{H I}}$  can be placed with 1,000 hr of observation. The limits on  $\tau_Q$  improves further and a lower limit can be placed on  $x_{\text{H I}}$  when the observation time is increased to 9,000 hr. These limits now are  $1.0 \leq \tau_Q/10^7 \text{ yr}) \leq 2.0$  and  $x_{\text{H I}} \geq 0.2$ . We see that there is a considerable improvement in parameter estimation if we have a brighter quasar with  $(\dot{N}_{\text{phs}}/10^{57} \text{ sec}^{-1}) = 8$ . We now have the limits  $0.5 \leq \tau_Q/10^7 \text{ yr}) \leq 2.5$  and  $x_{\text{H I}} \geq 0.1$  for 1000 hr of observation, and  $1.0 \leq \tau_Q/10^7 \text{ yr}) \leq 1.75$  and  $x_{\text{H I}} \geq 0.25$  for 9000 hr of observation.

We next consider the set e0 which corresponds to a later stage of growth  $(\tau_Q/10^7 \text{ yr}) = 2.8$ . We see that in this case the constraints on  $\tau_Q$  and  $x_{\text{H I}}$  are weaker compared to the set d where the quasar bubble is in an earlier stage of its growth. Here it is possible to place only a lower limit on  $\tau_Q$   $(\tau_Q/10^7 \text{ yr}) > 1.5$  for a quasar with  $(\dot{N}_{\text{phs}}/10^{57} \text{ sec}^{-1}) = 3$  and 1,000 hr of observation. These limits become  $2.0 \leq \tau_Q/10^7 \text{ yr}) \leq 5$  and  $x_{\text{H I}} \geq 0.15$  for 9,000 hr of observation. In case we have a brighter quasar  $(\dot{N}_{\text{phs}}/10^{57} \text{ sec}^{-1}) = 8$ , the limits are  $1.75 \leq \tau_Q/10^7 \text{ yr}) \leq 5$  and  $2.25 \leq \tau_Q/10^7 \text{ yr}) \leq 3.75$  for 1,000 and 9,000 hr of observation respectively, and  $x_{\text{H I}}$  can only be constrained ( $0.25 \leq x_{\text{H I}}$ ) with 9,000 hr of observation.

We next consider the possibility of a high neutral fraction ( $x_{\text{H I}} = 0.75$ ) for which a0, b0 and c0 respectively correspond to progressively increasing quasar age. Comparing the results with those for  $x_{\text{H I}} = 0.5$ , we find that in it is possible to place tighter constraints on  $\tau_Q$  and  $x_{\text{H I}}$  if the neutral fraction is higher. We find that it is possible to place an upper and a lower limit on  $\tau_Q$ , and a lower limit on  $x_{\text{H I}}$  in all the cases that we have considered. The constraints are tightest if the bubble is in the early stage of its growth, and we have  $0.5 \leq \tau_Q/10^7 \text{ yr}) \leq 2.25$  and  $x_{\text{H I}} \geq 0.1$  for 1,000 hr of observation for a quasar with  $(\dot{N}_{\text{phs}}/10^{57} \text{ sec}^{-1}) = 3$  and  $(\tau_Q/10^7 \text{ yr}) = 1.0$ . The constraints are further improved if we have longer observations or a brighter quasar.

We finally consider the set f0 which corresponds to a low neutral fraction ( $x_{\text{H I}} = 0.25$ ). In this case the bubble is not large enough for a detection in the early stage of its growth (Figure 4), and we have considered  $(\tau_Q/10^7 \text{ yr}) = 2.8$  which is in a later stage of its growth. We find that the prospects of constraining  $\tau_Q$  and  $x_{\text{H I}}$  are worse in comparison to the situation where we have a high neutral fraction. For a quasar with  $(\dot{N}_{\text{phs}}/10^{57} \text{ sec}^{-1}) = 3$  it is not possible to constrain  $x_{\text{H I}}$  even with 9,000 hr of observation, and it is possible to place only a lower limits  $(\tau_Q/10^7 \text{ yr}) \geq 1$  and  $(\tau_Q/10^7 \text{ yr}) \geq 1.75$  with 1,000 and 9,000 hr respectively. For a bright quasar  $(\dot{N}_{\text{phs}}/10^{57} \text{ sec}^{-1}) = 8$ , it is possible place constraints  $2 \leq \tau_Q/10^7 \text{ yr}) \leq 4$  and  $x_{\text{H I}} \leq 0.75$  with 9,000 hr of observation.

In summary, we find that the situation is most favourable for constraining  $\tau_Q$  and  $x_{\text{H I}}$  if we can detect a very luminous quasar in the early phase of its growth and also in the early stage of reionization when the neutral fraction is high.

As mentioned earlier in this section the anisotropy in the H II bubble's shape is determined by three parameters  $\dot{N}_{\text{phs}}/C$ ,  $x_{\text{H I}}/C$  and  $\tau_Q$ . We have assumed  $C = 30$  for both the filter and the bubble. It is quite possible that the actual clumping factor is different from  $C = 30$ . This will introduce a systematic uncertainty in parameter estimation. We consider two situations where the actual value of  $C$  for the bubble is different ( $C = 20$  and 40) than the

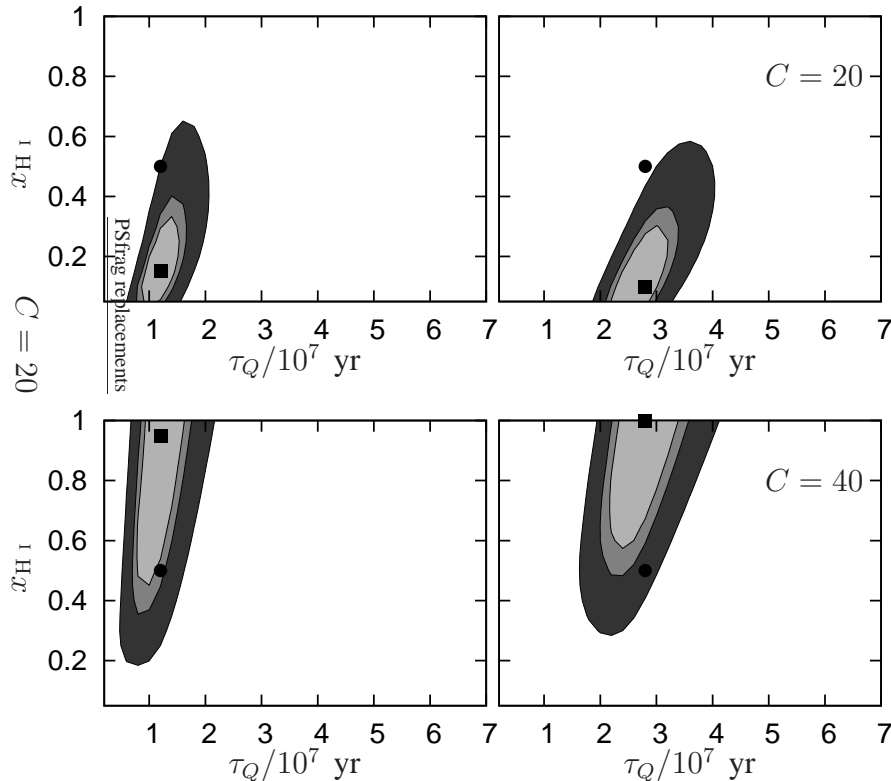


**Figure 8.** This shows the estimated parameters in a situation where the value of  $C$  assumed for the filter is different from the actual value in the IGM. Top and bottom panels correspond to the IGM having  $C = 20$  and  $40$  respectively. Left and right panels correspond to  $(\tau_Q/10^7 \text{ yr}) = 1.2$  and  $2.8$  respectively. The filter assumes  $C = 30$  in all cases. The bubble and the filter both have  $(\dot{N}_{\text{phs}}/10^{57} \text{ sec}^{-1}) = 8$ . The square in each panel shows the estimates from the search while the circle shows the actual input parameters. The shaded regions show the uncertainty ( $\Delta \text{SNR} = 1$ ) in the estimated parameters for 1,000, 4000 and 9,000 hr of observation.

filter ( $C = 30$ ) but the bubble and the filter both have same photon emission rate ( $(\dot{N}_{\text{phs}}/10^{57} \text{ sec}^{-1}) = 8$ ) in their models. Top and bottom panels of Figure 8 (corresponding to  $C = 20$  and  $40$  respectively) show the estimated values of parameters in these two different situations. We find that errors in  $C$  mainly affect the  $x_{\text{HI}}$ ,  $\tau_Q$  is largely unaffected by this. In a situation where the  $C$  in the IGM of the bubble is less ( $C = 20$ ) than what is assumed for the filter ( $C = 30$ ), the filter severely underestimates  $x_{\text{HI}}$  and this underestimation becomes more in the late stage ( $(\tau_Q/10^7 \text{ yr}) = 2.8$ ) of the growth than the early stage ( $(\tau_Q/10^7 \text{ yr}) = 1.2$ ). On the other hand when the  $C$  in the bubble’s IGM is more ( $C = 40$ ) than that of the filter, the  $x_{\text{HI}}$  is severely overestimated and this overestimation is more in the late stage ( $(\tau_Q/10^7 \text{ yr}) = 2.8$ ) of the bubble’s growth.

Similarly  $\dot{N}_{\text{phs}}$  estimated from the spectrum of the quasar could be off from the actual value. It will also have similar effects as the errors in  $C$  in parameter estimations.

#### 4 SIMULATING THE IONIZATION MAP

For our analytic estimates in the previous section we have considered that the H I density is uniform in the IGM around the quasar and there is no other ionizing source in the IGM except the target quasar. It is expected that in reality the IGM H I density will not be uniform and the stellar sources in the vicinity of the quasar will also contribute in ionizing the IGM. To study the detectability and

parameter estimation in a more realistic situation when all these effects are taken into account we have simulated the ionization map around the quasar using a semi-numerical formalism.

We have implemented the semi-numerical formalism proposed by Choudhury, Haehnelt & Regan (2009) for generating the ionization field at a given redshift. This uses an excursion-set formalism as introduced by Furlanetto, Zaldarriaga & Hernquist (2004).

It is currently believed that stars residing in galaxies are the major source of photons to reionize the universe (Choudhury & Ferrara, 2006; Choudhury, 2009). The early stages of reionization are driven by stars within halos of mass  $\sim 10^8 h^{-1} M_\odot$ . As the IGM becomes ionized, star formation within the smaller halos ( $M < 10^9 h^{-1} M_\odot$ ) is inhibited because of radiative feedback. Hence, it is sufficient to only include halos of mass  $M \geq 10^9 h^{-1} M_\odot$  to simulate the final stages of reionization. The smallest halo that is resolved in the simulation should be of mass  $M \leq 10^9 h^{-1} M_\odot$ . If at least 10 particles are required to constitute the smallest halo, then the particle mass should be  $\leq 10^8 h^{-1} M_\odot$ . This decides the mass resolution of our simulation.

We have generated the dark matter distribution at  $z = 8$  using a Particle Mesh Nbody code developed by Bharadwaj & Srikant (2004). The volume of the simulation is constrained by the 16 Gigabytes of memory available in our computer. We perform our simulation in a periodic box of size 85.12 Mpc (comoving) with  $1216^3$  grid points and  $608^3$  particles, with a mass resolution  $M_{\text{part}} = 7.275 \times 10^7 h^{-1} M_\odot$ .

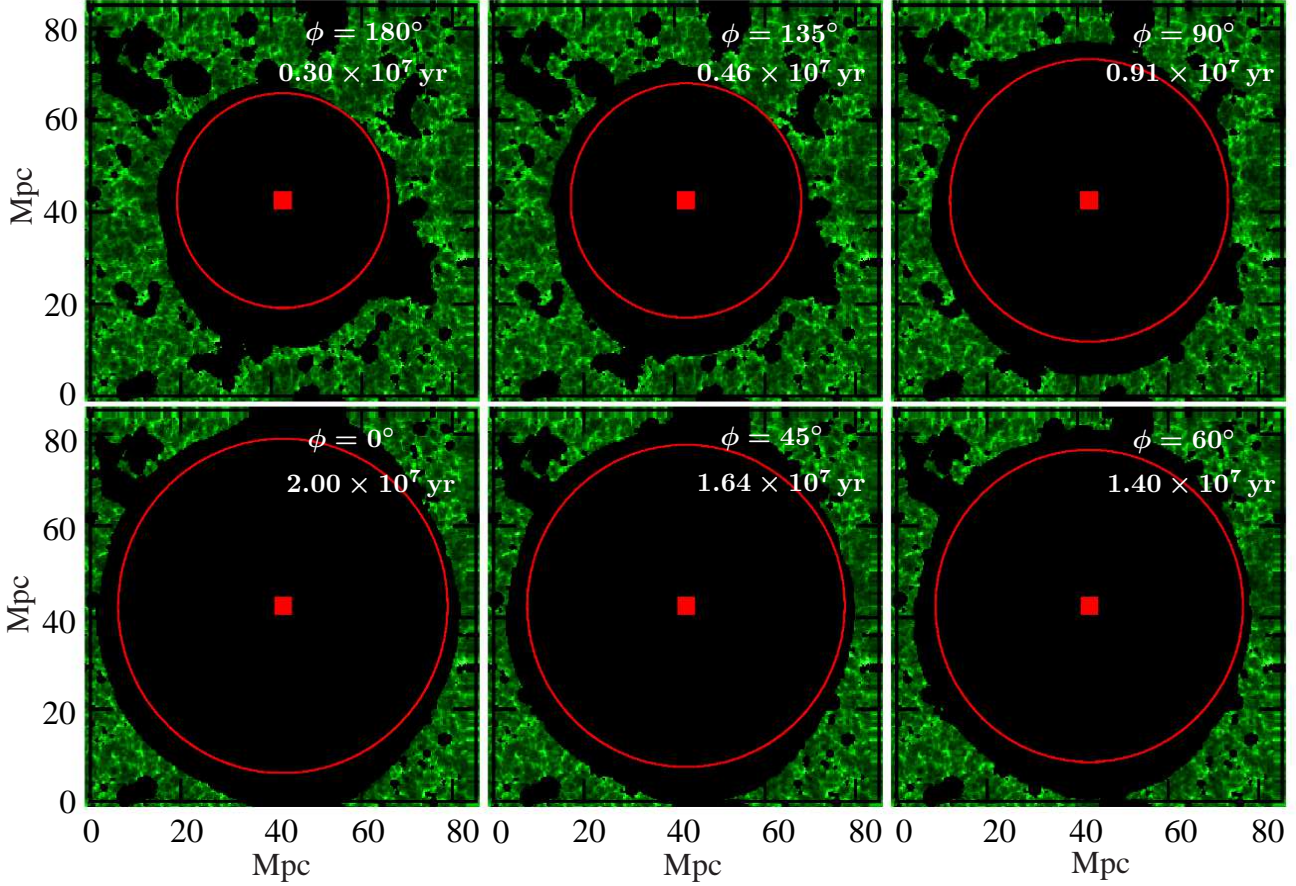


**Figure 9.** This shows a simulated quasar H II bubble with  $(\dot{N}_{phs}/10^{57} \text{ sec}^{-1}) = 1.3$  and  $x_{H\text{I}} = 0.5$  at different stages of its growth, as seen from the quasar's rest frame. The square in each panel shows the location of the quasar. The expected spherical size is shown by the circle. Panels are labelled with the corresponding quasar age and  $\phi$  is the angle with the LoS as defined in Figure 1 and eq. (3).

We identify halos within the simulation box using a standard Friend-of-Friend algorithm (Davis et al., 1985), with a fixed linking length  $b = 0.2$  (in units of mean inter particle distance) and minimum halo mass  $= 10M_{part}$ . We also compare the comoving number density of halos per unit logarithmic mass interval  $dn/d \ln M$  with the theoretical mass function at  $z = 8$  as predicted by Sheth & Tormen (2002) using the fitting function adopted from Jenkins et al. (2001). A good agreement is found over a wide mass range  $10^9 \lesssim M/(h^{-1}M_{\odot}) \lesssim 5 \times 10^{11}$ . The lower mass limit corresponds to the smallest halo mass.

The relation between the ionizing luminosity of a galaxy and its properties is not well known from observations. In the semi-numerical formalism adopted here, we assume that the ionizing luminosity from a galaxy is proportional to the mass of its halo. The number of ionizing photons contributed by a halo of mass  $M$  is given by,

$$N_{\gamma}(M) = N_{ion} \frac{M}{m_H}, \quad (17)$$

where  $m_H$  is the mass of a hydrogen atom and  $N_{ion}$  is a dimensionless constant. The value of  $N_{ion}$  is tuned so as to achieve the value  $x_{H\text{I}}$  desired in the simulation. In the semi-numerical formalism, a region is said to be ionized if the average number of photons reaching there exceeds average neutral hydrogen density at

that point. We have used a  $256^3$  grid with a grid spacing of 0.3325 Mpc for simulating the ionization maps.

The semi-numerical formalism provides a snapshot of the ionized IGM at a fixed instant of time  $t_s$ . We now briefly discuss how we have incorporated a quasar as an extra ionizing source in the simulation. The quasar is assumed to have ionizing luminosity  $\dot{N}_{phs}$  and age  $\tau$  at the instant  $t_s$ . We have identified the most massive halo ( $M \sim 5 \times 10^{11} h^{-1} M_{\odot}$ ) in the simulation as the quasar's location. We also shift the entire box with periodic boundary condition so as to bring the quasar into the centre of the field of view (FoV). In order to incorporate the quasar's H II bubble it is necessary to provide the simulation with a  $N_{\gamma, QSO}$ , the number of photons corresponding to the quasar at the instant  $t_s$ . We have used,

$$N_{\gamma, QSO} = \frac{4}{3} \pi \langle n_H \rangle x_{H\text{I}} r^3(\tau), \quad (18)$$

where  $r(\tau)$  is determined using eq. (2), *i.e.* the H II bubble would have a comoving radius  $r(\tau)$  if the hydrogen is uniformly distributed and there were no ionizing sources other than the quasar.

The quasar bubble actually produced in the simulation differs from this because of inhomogeneities in the hydrogen distribution and the presence of other ionizing sources. Further the density dependent non-uniform recombinations also change the bubble's size and shape in the cases where this effect is included. In general, we

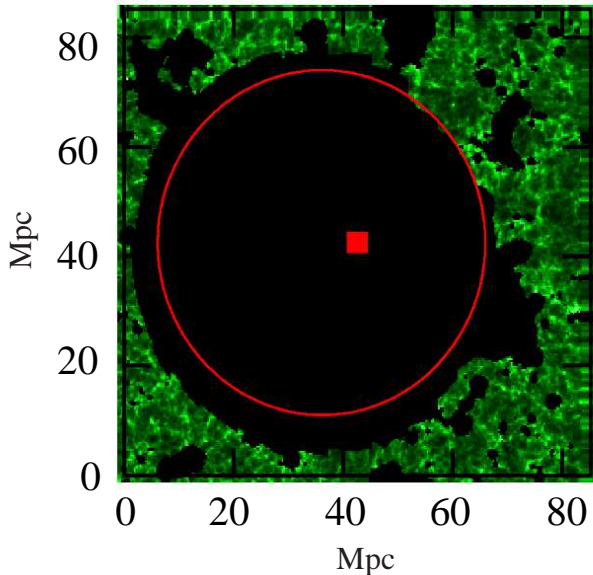


**Figure 10.** This shows the apparent shape of the H II bubble around a quasar after the snapshots at different stages of its growth (Figure 9) have been stacked together. The square shows the location of the quasar. The curve shows the expected apparent shape of the bubble. The observer is on the left of the figure.

find the simulated H II bubbles are bigger than predicted by the eq. (2), mainly because of the contributions of other ionizing sources near the quasar. Figure 9 provides a visual impression of a suite of simulations with  $(\dot{N}_{phs}/10^{57} \text{ sec}^{-1}) = 1.3$ ,  $x_{\text{H I}} = 0.5$  and different values of  $\tau$ . We notice that there is a particularly large deviation from the expected bubble size at the early stages of the bubble’s growth. The actual bubble is much larger than that expected from the  $N_{\gamma, \text{QSO}}$  that we have assigned to the quasar. The massive halos, which are the only other ionizing sources besides the quasar, are preferentially clustered in the vicinity of the quasar which is located in the most massive halo in the simulation. The ionizing photons from these halos outnumber those from the quasar in the early stages, and consequently the actual bubble is much larger than expected. This discrepancy persists even in the later stages, however it is not so pronounced. A similar observation has been reported by Datta et al. (2012) in their radiative transfer simulations.

A distant observer sees different parts of the H II bubble in different stages of its growth. We have assumed that the dark matter distribution and the global  $x_{\text{H I}}$  do not change within the look back time across the bubble. We have used eq. (2) and (3) to determine  $r$  as a function of  $\phi$ . We then choose sections each through a different member of the suite of simulations (Figure 9). Each section corresponds to a different value of  $r$  and  $\tau$  as determined by eq. (2) and (3). These sections are stacked together to produce the bubble’s apparent shape as seen by the distant observer. Figure 10 shows the apparent shape generated by stacking sections selected from the Figure 9.

Our simulations spans a redshift interval  $\Delta z = 0.28$  along the LoS. We have made a simplifying assumption that the dark matter distribution and the variation in  $x_{\text{H I}}$  across our simulation box can be ignored. Analytic estimates (for details see Appendix A and Results of Paper II) show that the effects ignored here make a 5% or less contribution. Further, simulations (Datta et al., 2012) also reveal similar findings, justifying the assumptions made here.

set	$\dot{N}_{phs}/10^{57}$ ( $\text{sec}^{-1}$ )	$x_{\text{H I}}$	$\tau_Q/10^7$ (yr)
A	1.3	0.50	2.00
B	1.3	0.50	3.00
C	1.3	0.75	1.50
D	1.3	0.75	3.50
E	3.0	0.50	0.75
F	3.0	0.75	0.50

**Table 3.** This tabulates the quasar and IGM parameters for which the H II bubbles have been simulated.

The GMRT FoV at 151 MHz has a full width at half maxima (FWHM) =  $2.28^\circ$  while our simulation box only subtends an angle  $0.53^\circ$  on the sky and 4.8 MHz along the LoS at redshift  $z = 8$ . Thus the simulation box will not be able to replicate the full GMRT FoV and can accommodate a bubble of maximum radius  $\sim 40$  Mpc, which subtends  $\sim 0.5^\circ$ . Maselli et al. (2007) predict the comoving radius of quasar generated H II regions to be  $\sim 45$  Mpc at  $z = 6.1$  with  $x_{\text{H I}} = 0.1$ . The size is expected to be less at  $z = 8$ . Our simulation box is thus large enough to host H II bubbles in the relevant size range at this redshift. The simulation adequately replicate the H I fluctuations in the vicinity of the bubble, however the H I fluctuations at large angular separation from the bubble’s centre are missing. The H I fluctuations are some what underestimated as a consequence (see Datta et al. 2008 for more details).

The simulated H I maps were converted to GMRT visibilities which were then used for matched filter bubble detection following the procedure detailed in Datta et al. (2008).

## 5 RESULTS

We have created six different realizations of the dark matter distribution using the PM Nbody code. These were used to generate six independent realizations of the quasar bubble for each of the parameter sets given in Table 3. We have seen that it is possible to constrain different regions of the  $x_{\text{H I}} - \tau_Q$  parameter space by observing quasars in different stages of growth. Ideally we would like to simulate bubbles in different stages of the growth for a variety of  $\dot{N}_{phs}$  and  $x_{\text{H I}}$ . However our choice of parameters are restricted by the condition that the bubble should be small enough ( $< 40$  Mpc) to be contained within the simulation box, while it should also be large enough for a  $3\sigma$  detection (Figure 4). Figure 11 shows the simulated H II bubble for each set of the parameters listed in Table 3. The images shown in the figure all correspond to the same realization, with uniform recombination. Three sets of simulations A, B and E have  $x_{\text{H I}} = 0.5$ . The sets C, D and F have a higher neutral fraction ( $x_{\text{H I}} = 0.75$ ). We are unable to simulate any situation with a low  $x_{\text{H I}}$  because the bubble size would have to be larger than our box for a detection to be possible. The sets A, B, C and D have a quasar luminosity  $(\dot{N}_{phs}/10^{57} \text{ sec}^{-1}) = 1.3$  which is the same as the quasar detected by Mortlock et al. (2011). This luminosity is relatively low in comparison to the values that we have considered earlier. The quasar has to be observed at a late stage for a detection to be possible, and we expect a large bubble. The bubble centre will be shifted from the quasar for A and C where the quasar is somewhat younger with  $(\tau_Q/10^7 \text{ yr}) = 2.0$  and  $1.5$  respectively compared to B and D which have  $(\tau_Q/10^7 \text{ yr}) = 3.0$  and  $3.5$  respectively. The bubbles are also expected to be compressed in sets

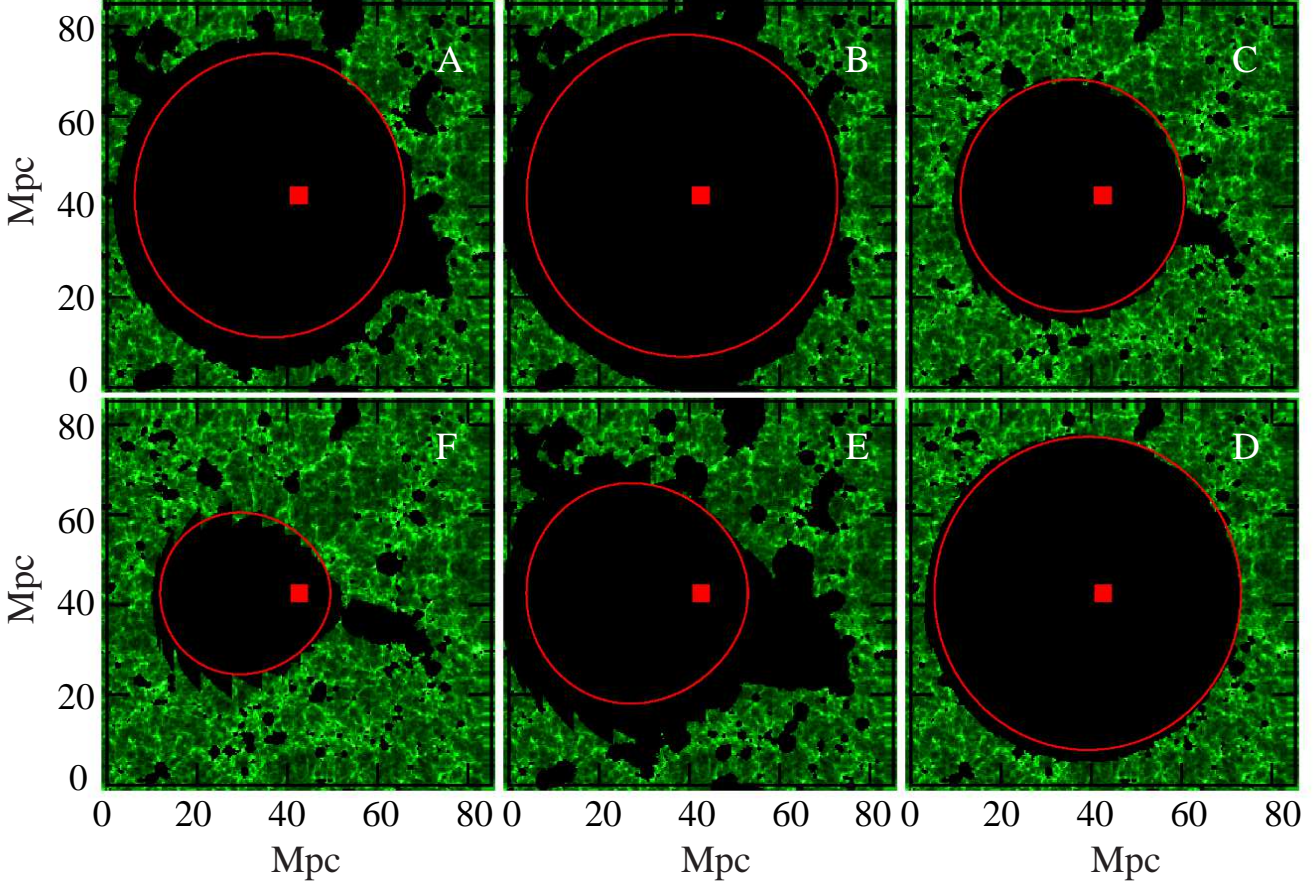


**Figure 11.** This shows the simulated bubbles for different sets of quasar and IGM parameters as tabulated in Table 3 considering uniform recombination in the IGM. The square in each panel represents the location of the quasar. The curve shows the expected bubble shape. In all panels the observer is to the left side of the box.

A and C, which is distinctly visible in these images. The bubble is expected to be nearly spherical in sets B and D.

We see that the simulated bubbles are in reasonable agreement with what is expected, though the simulated bubbles are nearly always larger. This discrepancy arises due to the extra ionizing photons contributed by the halos located within the bubble. The number of ionizing photons contributed by these halos is proportional to the ionization fraction  $(1 - x_{\text{H I}})$ . Consequently the discrepancy between the expected bubble size and that obtained in the simulations is larger for  $x_{\text{H I}} = 0.5$  in comparison to  $x_{\text{H I}} = 0.75$ . Further, the bubble's boundary is distorted because the bubble gets merged with the ionized regions produced by halos located in the periphery of the bubble. These distortions are particularly important when the halos located near the bubble's boundary contribute a significant fraction of the total ionizing photons within the bubble. We thus expect these distortions to be relatively important when the bubble is in the early stage of growth and we have a low neutral fraction, whereas we expect the distortions to be relatively less important when the bubble is in a later stage and in an IGM with a higher  $x_{\text{H I}}$ .

The sets E and F have  $(\dot{N}_{\text{phs}}/10^{57} \text{ sec}^{-1}) = 3$ , and the quasar's ages are smaller  $((\tau_{\text{Q}}/10^7 \text{ yr}) = 0.75 \text{ and } 0.50)$  in comparison to sets A,B,C and D discussed earlier. We expect the bubbles to be elongated along the LoS in these two sets, and this is clearly visible in Figure 11. However, the bubble's shape is severely distorted in E where the neutral fraction is less compared to F. We

expect such distortions to severely affect parameter estimation. We see that the distortion present in E also persists for F, however the relative contribution is smaller. We may expect the impact of this distortion on parameter estimation to be less severe in F as compared to E.

Figure 12 shows images from simulations with inhomogeneous recombination. We see that the bubbles are larger in comparison to the situation with uniform recombination. It is possible to understand this by noting that in these models the dense regions in the IGM remain neutral through enhanced recombination, and only the low density regions are ionized. Consequently, a larger volume has to be ionized in order to achieve a particular value of the mass averaged neutral fraction  $x_{\text{H I}}$ . Further, the contrast between the bubble and the IGM outside is reduced, and the bubble's boundary is more distorted.

For a fixed set of parameters, we expect the simulated bubble to differ from one realization to the next. Figure 13 shows two different realizations of the simulated bubble for the parameter set A in addition to the realization shown in Figure 11. We see that in all the realizations the bubble appears larger than expected. The distortions, we notice, can vary significantly from one realization to the next. In particular, the right panel of Figure 13 shows a realization where an extraneous ionization source is so aligned that it causes the ionized bubble to appear elongated along the LoS. Recollect that the bubble is expected to appear compressed in set A. Such distortions are a source of concern for parameter estimation.

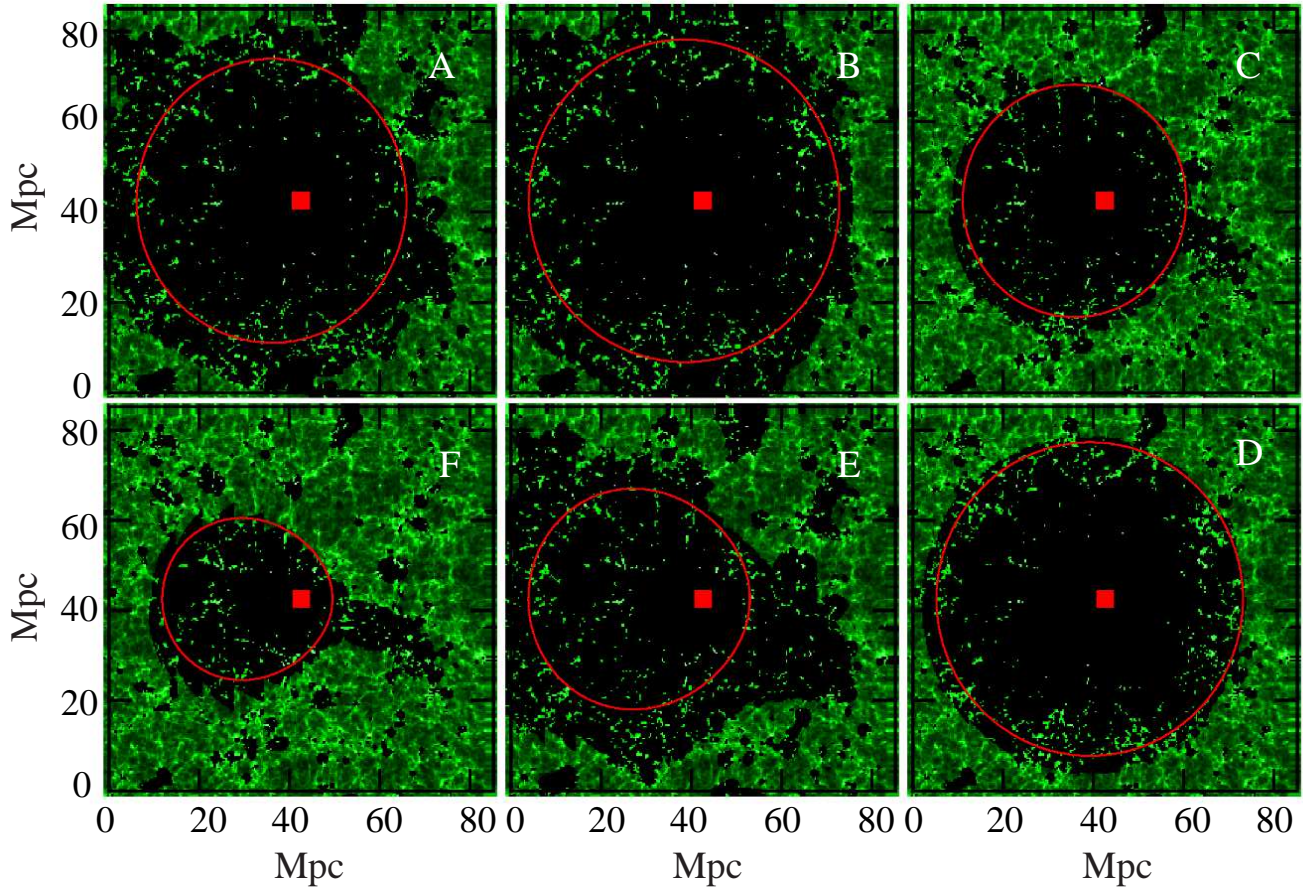


Figure 12. Similar to Figure 11 considering non-uniform recombination in the IGM.

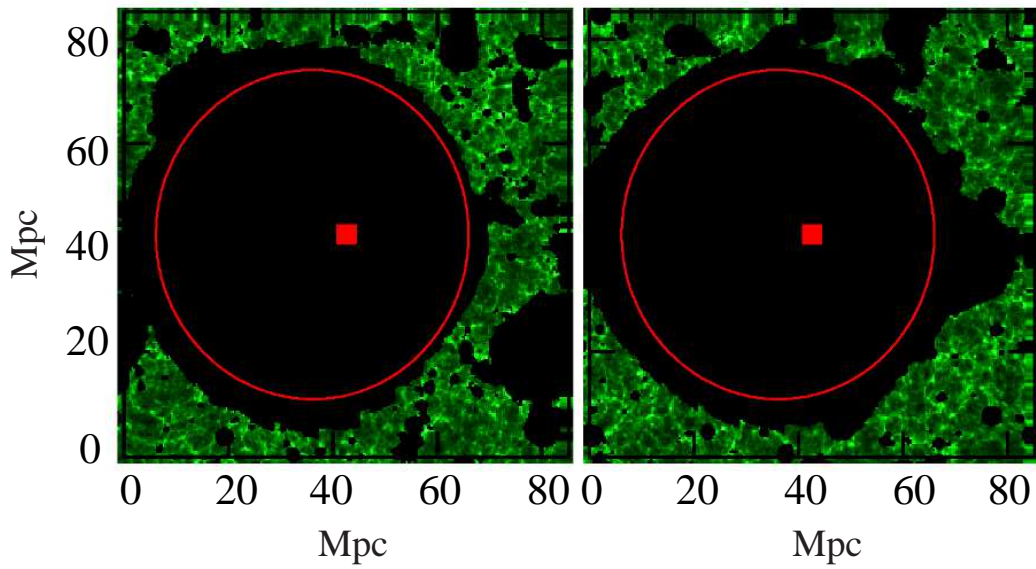
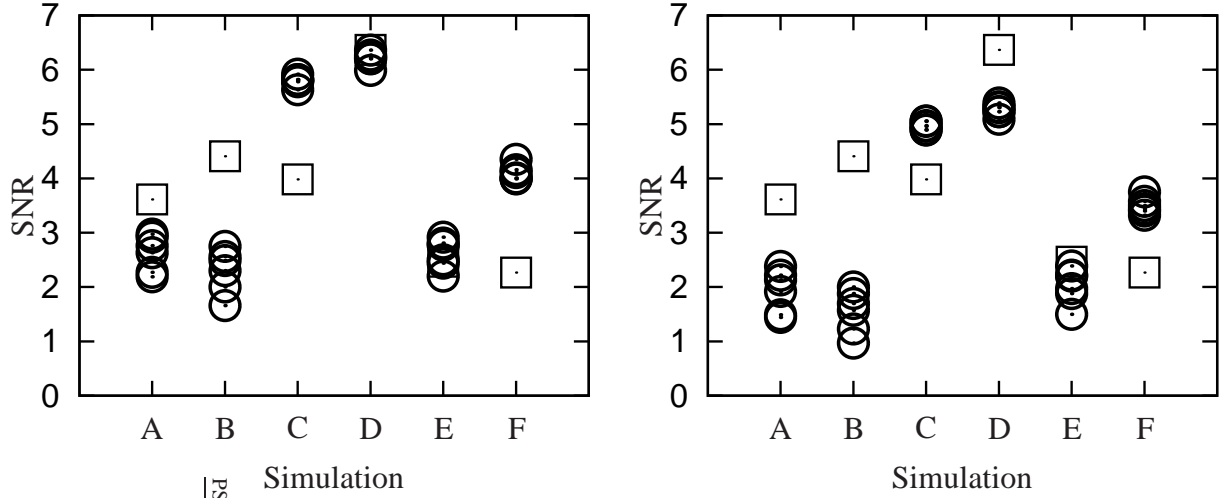
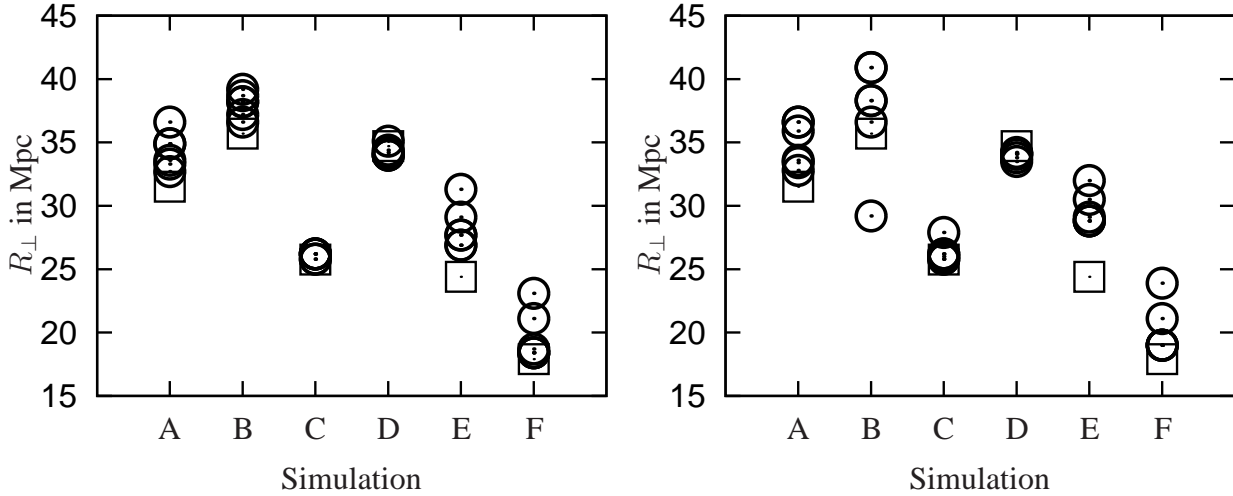


Figure 13. This shows two different realizations of the simulated H II bubbles having the same set of parameters (set A). The effect of the photon contribution from neighbouring halos is severe in the right panel as compared to the bubble in the left panel. The curve shows the expected bubble shape. In both panels the observer is to the left of the box.



**Figure 14.** This shows the SNR for 1,000 hr of observation for the different sets of parameters in Table 3. The squares indicate the analytic estimates and the circles represent the SNR estimated from different realizations of the simulations. Left and right panels correspond to simulations with uniform and non-uniform recombinations respectively.



**Figure 15.** This shows the bubble size estimated from matched filter search on simulated H II bubbles for the different sets of parameters in Table 3. The squares indicate the analytic estimates of  $R_{\perp}$  and the circles represent the same estimated from different realizations of the simulations. Left and right panels correspond to the simulations with uniform and non-uniform recombinations respectively.

Distortions in the H II bubble and fluctuations in the H I distribution outside the bubble will affect the SNR for bubble detection and also the radius  $R_{\perp}$  estimated from the best matched filter. Figure 14 shows a comparison of the expected SNR from our analytic estimates and the SNR obtained from the simulations. We note that the expected SNR has values 2.46 and 2.26 for the parameters sets E and F, and a  $3\sigma$  detection is not possible with 1,000 hr of observation. We need 1,500 and 1,750 hr of observation for a  $3\sigma$  detection for E and F respectively.

We find that the SNR is below the expected value in cases A and B, whereas it is comparable to the expected value in D and E, and it is larger than the expected value in C and F. We note that the reduction in SNR seen in A and B may be an artifact of the limited volume of our simulation where the bubble becomes comparable to the box size. The sets C and F where the SNR is

larger than the expected value both correspond to an early stage of the growth in a highly neutral IGM ( $x_{\text{H I}} = 0.75$ ). We also find that there is a significant scatter in the SNR values amongst the different realizations. This scatter is relatively smaller for the sets which have a higher neutral fraction  $x_{\text{H I}} = 0.75$  where we expect the halos to make a relatively smaller contribution to the ionizing photons. The scatter in the SNR remains the same even when we consider non-uniform recombination. However, the overall values of the SNR obtained from the different realizations are now slightly reduced with respect to uniform recombination. The fact that the SNR goes down if we introduce non-uniform recombination is a consequence of the lower contrast between the ionized bubble and the IGM outside.

Figure 15 shows the bubble radius  $R_{\perp}$  estimated from the best matched filter for the simulations compared with the analytic es-

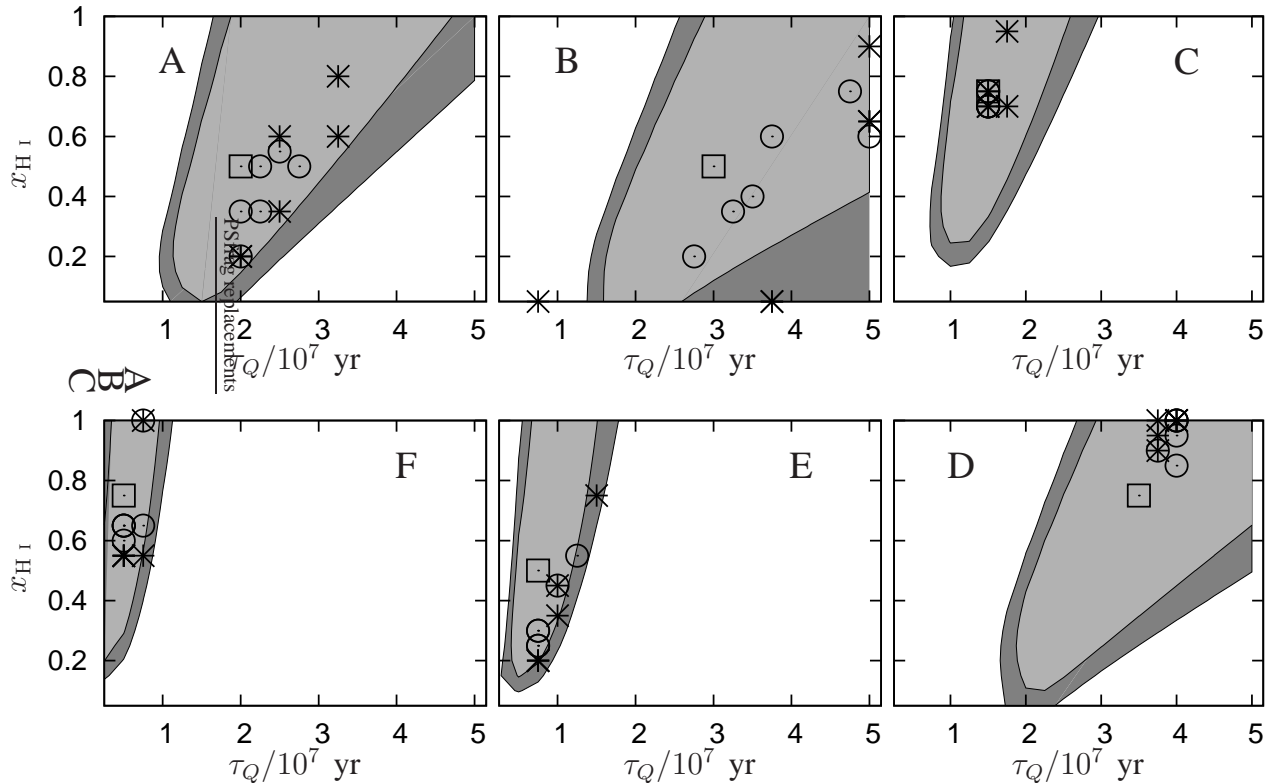


**Figure 16.** This shows the location of the peak SNR for the different sets of parameters in Table 3. The square in each panel indicates the actual value of  $x_{\text{H I}}$  and  $\tau_{\text{Q}}$ , the circles and stars correspond to the estimated values from different realizations of the simulations with to uniform and non-uniform recombination respectively. The shaded regions correspond to the analytic estimates of the uncertainty ( $\Delta\text{SNR} = 1$ ) for 4,000 and 9,000 hr of observations.

timates. As discussed earlier, we find that the simulated bubble is nearly always larger than what is expected from estimates. This discrepancy is particularly noticeable ( $\sim 15\text{--}20\%$ ) in the cases which have a lower neutral fraction  $x_{\text{H I}} = 0.5$  and where we expect the halos to make a relatively larger contribution. Further as noted earlier the discrepancy is larger in the simulations with non-uniform recombination in comparison to those with uniform recombination.

We next use the simulated H II bubbles to analyze parameter estimation. Figure 16 shows the parameter values corresponding to the peak SNR for the different realizations of the simulations. We see that the values of  $\tau_{\text{Q}}$  and  $x_{\text{H I}}$  recovered from the simulations are different from the actual age and neutral fraction. Reason for these deviations are the distortions in the bubble due to the other ionizing sources and the inhomogeneities in the IGM. Figure 16 also shows analytic predictions of the uncertainties ( $\Delta\text{SNR} = 1$ ) in the estimated values of  $x_{\text{H I}}$  and  $\tau_{\text{Q}}$  for the different sets (Table 3) considering 4,000 and 9,000 hr of observation. We have not shown 1,000 hr observation as bubble detection is not possible in this observation time for a few of the cases (E and F) that we have considered. We find that most of the simulations give parameter estimates which lie within the region corresponding to  $\Delta\text{SNR} = 1$  for 9,000 hr of observation. We first discuss the sets E and F where the bubble is at a very early stage of its growth and is rather small. We require more than 1,000 hr of observation for a  $3\sigma$  detection. We find that in these two sets the neutral fraction is underestimated in almost all the realizations. This is a consequence of the fact that the actual bubble is almost always larger than expected (Figure 15) due to the presence other ionizing sources within the bubble. This effect is more pronounced when the IGM neutral fraction is low

( $x_{\text{H I}} = 0.5$  in set E). This discrepancy in the bubble size only affects the estimated neutral fraction. The bubble in its early stage is very sensitive to  $\tau_{\text{Q}}$  through the anisotropy  $\eta$  and the shift parameter  $s$  (Figure 5) which are not severely affected by the overall size of the bubble. We find that in sets E and F the quasar age inferred from the simulations is quite close to the actual value.

We next consider A, B, C and D which correspond to later stages of the bubble's growth. We find that the scatter in the values of  $x_{\text{H I}}$  and  $\tau_{\text{Q}}$  inferred from the simulations is considerably smaller for a high neutral fraction  $x_{\text{H I}} = 0.75$  (C and D) as compared to  $x_{\text{H I}} = 0.5$  (A and B) where the halos make a relatively larger contribution to the ionizing photons. In sets A and B the estimated  $x_{\text{H I}}$  is found to be uniformly scattered around the actual value. However, the value of  $\tau_{\text{Q}}$  is overestimated in the majority of the simulations. In set D we find that both  $x_{\text{H I}}$  and  $\tau_{\text{Q}}$  are slightly overestimated in the simulations, while nearly all the simulated values lie very close to the actual value in set C.

In summary, our analysis is based on the assumption that the SNR of the estimator will peak when the parameters of the filter exactly match those of the bubble that is actually present in the data. The statistical uncertainty of the estimator will, however, cause the peak to shift introducing an uncertainty in parameter estimation. Further, distortions in the shape and size of the bubble due to other ionizing sources and the inhomogeneities in the IGM will also cause the peak SNR to shift, introducing further uncertainties in parameter estimation. In our work we have used the criteria  $\Delta\text{SNR} = 1$  to analytically estimate the statistical uncertainties. Further, we have used simulations to assess the effect of the distortions. We find that the statistical uncertainties are large in most of the situations

that we have considered, and hence these can be used to determine the uncertainties in the estimated parameter. We find that reliable parameter estimation is possible using H II bubbles for which a  $3\sigma$  detection is possible in 1,000 hr of observation. Smaller bubbles, which require longer observations, do not provide very reliable estimates of  $x_{\text{H I}}$ , they can however be used to obtain a reliable estimate of  $\tau_Q$ .

At the moment we do not have a rigorous justification for the criteria  $\Delta\text{SNR} = 1$  which we have adopted here. A more detailed statistical analysis involving extensive simulations with large number of realizations of both the statistical fluctuations as well as the distortions are required. At the moment this is beyond the computational power available to us. However, 21-cm observations of ionized bubbles hold the promise of allowing us to probe the age of the quasar and the neutral fraction of the IGM, and we plan to pursue such simulations in future.

## 6 ACKNOWLEDGMENTS

We would like to thank the anonymous reviewer for providing us with constructive comments and suggestions which helped to improve the paper. Suman Majumdar would like to thank Kanan Kumar Datta for useful discussions and programming related helps during this work. Suman Majumdar would like to acknowledge Council of Scientific and Industrial Research (CSIR), India for providing financial assistance through a senior research fellowship (File No. 9/81 (1099)/10-EMR-I). Suman Majumdar would also like to thank Harish-Chandra Research Institute, Allahabad, for their warm hospitality during a visit in February, 2011, when this work was initiated.

## References

- Ali, S. S., Bharadwaj, S., & Chengalur, J. N. 2008, MNRAS, 385, 2166
- Bernardi, G., de Bruyn, A. G., Brentjens, M. A., et al. 2009, AAP, 500, 965
- Bharadwaj, S., & Srikant, P. S. 2004, Journal of Astrophysics and Astronomy, 25, 67
- Bolton, J. S., Haehnelt, M. G., Warren, S. J., Hewett, P. C., Mortlock, D. J., Venemans, B. P., McMahon, R. G., Simpson, C. 2011, MNRAS, 416, L70
- Choudhury, T. R., Ferrara, A., 2006, Cosmic Polarization, Editor - R. Fabbri(Research Signpost), p. 205, arXiv:astro-ph/0603149
- Choudhury, T. R., 2009, Current Science, 97, 6, 841
- Choudhury, T. R., Haehnelt, M. G., & Regan, J. 2009, MNRAS, 394, 960
- Datta, K. K., Bharadwaj, S., & Choudhury, T. R., 2007, MNRAS, 382, 109
- Datta, K. K., Majumdar, S., Bharadwaj, S., & Choudhury, T. R., 2008, MNRAS, 391, 1900
- Datta, K. K., Bharadwaj, S., & Choudhury, T. R. 2009, MNRAS, 399, L132
- Datta, K. K., Mellema, G., Mao, Y., Iliev, I. T., Shapiro, P. R., Ahn, K. 2012, MNRAS, 424, 1877
- Datta, K. K., Friedrich, M. M., Mellema, G., Iliev, I. T., & Shapiro, P. R. 2012, MNRAS, 424, 762
- Davis, M., Efstathiou, G., Frenk, C. S., & White, S. D. M. 1985, ApJ, 292, 371
- Fan, X., Strauss, M. A., Schneider, D. P., et al. 2003, AJ, 125, 1649
- Furlanetto, S. R., Zaldarriaga, M. & Hernquist, L. 2004, ApJ, 613, 1
- Geil, P. M., Wyithe, J. S. B., Petrovic, N., & Oh, S. P. 2008, MNRAS, 390, 1496
- Gnedin, N. Y., & Ostriker, J. P. 1997, ApJ, 486, 581
- Haehnelt, M. G., Natarajan, P., & Rees, M. J. 1998, MNRAS, 300, 817
- Haiman, Z., & Hui, L. 2001, ApJ, 547, 27
- Jarosik, N. et al. 2011, ApJS, 192, 14
- Jenkins, A., Frenk, C. S., White, S. D. M., Colberg, J. M., Cole, S., Evrard, A. E., Couchman, H. M. P., & Yoshida, N. 2001, MNRAS, 321, 372
- Komatsu, E. et al. 2011, ApJS, 192, 18
- Lu, Y., & Yu, Q. 2011, ApJ, 736, 49
- Majumdar, S., Bharadwaj, S., Datta, K., K., & Choudhury, T. R. 2011, MNRAS, 413, 1409
- Maselli, A., Gallerani, S., Ferrara, A., & Choudhury, T. R. 2007, MNRAS, 376, L34
- Mitra, S., Choudhury, T. R., & Ferrara, A. 2011, MNRAS, 413, 1569
- Mortlock, D., J., et al. 2011, Nature, 474, 7353
- Sethi, S., & Haiman, Z. 2008, AJ, 673, 1S
- Shapiro, P. R., & Giroux, M. L. 1987, ApJL, 321L, 107S
- Sheth, R. K., & Tormen, G. 2002, MNRAS, 329, 61
- Swarup G., Ananthakrishnan S., Kapahi V.K., Rao A.P., Subramanya C.R., Kulkarni V.K., 1991 Curr.Sci., 60,95
- White, R. L., Becker, R. H., Fan, X., & Strauss, M. A. 2003, AJ, 126, 1
- Willott, C. J., Delorme, P., Omont, A., et al. 2007, AJ, 134, 2435
- Willott, C. J., Albert, L., Arzoumanian, D., et al. 2010, AJ, 140, 546
- Worseck, G., & Wisotzki, L. 2006, AAP, 450, 495
- Wyithe, J. S. B., & Loeb, A. 2004, ApJ, 610, 117
- Wyithe, J. S. B., Loeb, A., & Barnes, D. G. 2005, ApJ, 634, 715
- Yu, Q. & Lu, Y. 2005, ApJ, 620, 31
- Yu, Q. 2005, ApJ, 623, 683